Thermodynamic Characteristics of Downdrafts in Tropical Cyclones as Seen in Idealized Simulations of Different Intensities

JOSHUA B. WADLER,[a,b] DAVID S. NOLAN,[c] JUN A. ZHANG,[a,b] AND LYNN K. SHAY[c]

[a] *NOAA/Atlantic Oceanographic and Meteorological Laboratory/Hurricane Research Division, Miami, Florida*
[b] *Cooperative Institute for Marine and Atmospheric Studies, University of Miami, Miami, Florida*
[c] *Rosenstiel School of Marine and Atmospheric Sciences, University of Miami, Miami, Florida*

(Manuscript received 6 January 2021, in final form 3 August 2021)

ABSTRACT: The thermodynamic effect of downdrafts on the boundary layer and nearby updrafts are explored in idealized simulations of category-3 and category-5 tropical cyclones (TCs) (Ideal3 and Ideal5). In Ideal5, downdrafts underneath the eyewall pose no negative thermodynamic influence because of eye–eyewall mixing below 2-km altitude. Additionally, a layer of higher θ_e between 1- and 2-km altitude associated with low-level outflow that extends 40 km outward from the eyewall region creates a ''thermodynamic shield'' that prevents negative effects from downdrafts. In Ideal3, parcel trajectories from downdrafts directly underneath the eyewall reveal that low-θ_e air initially moves radially inward allowing for some recovery in the eye, but still enters eyewall updrafts with a mean θ_e deficit of 5.2 K. Parcels originating in low-level downdrafts often stay below 400 m for over an hour and increase their θ_e by 10–14 K, showing that air–sea enthalpy fluxes cause sufficient energetic recovery. The most thermodynamically unfavorable downdrafts occur ~5 km radially outward from an updraft and transport low-θ_e midtropospheric air toward the inflow layer. Here, the low-θ_e air entrains into the updraft in less than 5 min with a mean θ_e deficit of 8.2 K. In general, θ_e recovery is a function of minimum parcel altitude such that downdrafts with the most negative influence are those entrained into the top of the inflow layer. With both simulated TCs exposed to environmental vertical wind shear, this study underscores that storm structure and individual downdraft characteristics must be considered when discussing paradigms for TC intensity evolution.

SIGNIFICANCE STATEMENT: It is known that downdrafts transport cool and dry air into the hurricane boundary layer, where it can enter the eyewall and weaken the storm. Simulated hurricanes are used to understand how the effects of individual downdrafts are related to their location within the storm and the hurricane's structure. Downdrafts near the upper part of the boundary layer have the greatest weakening effect, while downdrafts that reach the surface are mitigated by energy transferred from the ocean. Additionally, when warm and moist air is transported away from the eyewall aloft, it shields the boundary layer from unfavorable downdraft air, mitigating its effect. The results highlight the importance of storm structure and air–sea interactions for understanding how downdrafts influence hurricane intensity.

KEYWORDS: Convection; Hurricanes; Updrafts/downdrafts; Tropical cyclones; Air-sea interaction; Thermodynamics

1. Introduction

The multiscale problem of understanding tropical cyclone (TC) intensity change still challenges researchers and operational meteorologists (e.g., Marks and Shay 1998; Rogers et al. 2006, 2013a; DeMaria et al. 2014, 2021; Cangialosi et al. 2020; Trabing and Bell 2020; Zawislak et al. 2021). Recent initiatives to address this issue have focused on the kinematic and thermodynamic influence of deep layer environmental wind shear (defined as difference in environmental winds between 200 and 850 hPa) on vortex structure. One emerging paradigm is that ventilation, the mixing of dry environmental air into the TC circulation, is one of the main mechanisms for environmental wind shear to influence TC intensity (e.g., Riemer et al. 2010, 2013; Tang and Emanuel 2010, 2012; Ge et al. 2013; Molinari et al. 2013; Alland et al. 2017, 2021a,b; Colomb et al. 2019). However, the pathways by which dry air entrains into updrafts and weaken TCs have not been definitively established. The goal of this paper is to show these pathways explicitly.

In a sheared TC, the tilt of the vortex leads to the entrainment of dry midtropospheric environmental air into the circulation, which can influence the inner core through low-level and midlevel ventilation. In midlevel ventilation, the dry midtropospheric air can directly mix with the eyewall, effectively weakening the efficiency of the TC heat engine (Tang and Emanuel 2010, 2012). In low-level ventilation, the dry midtropospheric air is transported to the boundary layer via downdrafts. Low-level ventilation was a prevailing process in two recent modeling studies by Riemer et al. (2010, 2013), which diagnosed that when a mature TC is exposed to shear, downdrafts underneath quasi-persistent rainbands outside the eyewall region transport low-moist-entropy (θ_e; also referred to as equivalent potential temperature) air to the inflow layer. As

Corresponding author: Joshua B. Wadler, joshua.wadler@noaa.gov

DOI: 10.1175/JAS-D-21-0006.1

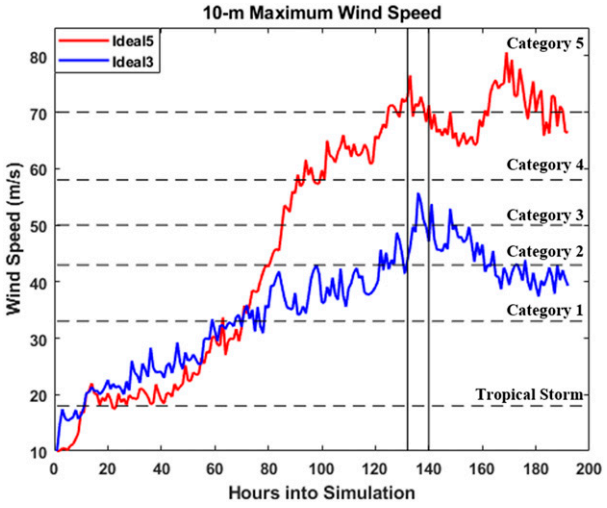

FIG. 1. The 10-m maximum wind speed based on hourly output from the Ideal3 and Ideal5 simulations. The solid vertical lines represent the start and end times of the restart simulation used for obtaining data at 2-min outputs. The horizontal dashed lines represent categories (labeled on the right) on the Saffir–Simpson intensity scale.

with midlevel ventilation, low-θ_e air in the inflow layer can entrain into the eyewall updrafts and decrease the efficiency of the TC heat engine.

With convective downdrafts in TCs being widely studied using observations (e.g., Barnes et al. 1983; Powell 1990; Barnes and Powell 1995; Didlake and Houze 2009, 2013; Cione et al. 2000, 2013; Eastin et al. 2012; Barnes and Dolling 2013; Molinari et al. 2013; Dolling and Barnes 2014; Zhang et al. 2017; Nguyen et al. 2019), recent efforts have tried to further understand their thermodynamic impact on the boundary layer. Molinari et al. (2013) used flight-level data and dropsondes in Tropical Storm Edouard (2002) to confirm the existence of convective downdrafts and coincident 4–6-K-lower θ_e than that observed after the boundary layer recovery process. Rogers et al. (2016) and Zawislak et al. (2016) studied the evolution of Hurricane Edouard (2014) and found that in the period prior to intensification, broad subsidence upshear dried the midlevels and limited the amount of precipitation. In a study of Tropical Cyclones Bertha and Cristobal (2014), Nguyen et al. (2017) found that after lateral advection into the upshear quadrants, dry environmental air interacted with moist convection leading to mesoscale and convective downdrafts into the boundary layer. With a new technique of collocating profiles of thermodynamic observations obtained from dropsondes with kinematic observations obtained from pseudo-dual-Doppler radar observations on the NOAA WP-3D (P-3), Wadler et al. (2018a) showed that in Hurricane Earl (2010), strong convective downdrafts (i.e., $>2\,\mathrm{m\,s^{-1}}$) in the eyewall contained θ_e values that were similar to other boundary layer θ_e values at that radius where no downdraft was observed. The downdrafts with the most detrimental thermodynamic characteristics were broad mesoscale downdrafts in the upshear-left (USL) quadrant that were not associated with deep convection. To the authors' knowledge, no numerical study has linked downdraft characteristics (e.g., strength, storm-relative location) to the thermodynamic impact they have on the boundary layer and nearby updrafts.

When downdrafts transport low-θ_e air to the boundary layer, there is a chance for θ_e recovery. In the Molinari et al. (2013) and Wadler et al. (2018a) case studies, as well as a case study of Hurricane Edouard (2014) by Zhang et al. (2017), bulk boundary layer recovery calculations (i.e., a single layer boundary layer model) suggested that, in intensifying storms, the boundary layer was able to recover from low-θ_e air via the air–sea enthalpy fluxes by the time parcels traversed from the USL to the downshear-right (DSR) quadrants. The amount of recovery in each case is related to the upper-ocean thermal and salinity structure, which plays a critical role in determining the magnitude of the air-sea enthalpy fluxes (e.g., Shay et al. 2000; Jaimes and Shay 2009, 2010; Jaimes et al. 2015; Rudzin et al. 2018, 2019; Hlywiak and Nolan 2019; Balaguru et al. 2020).

While observational studies are useful for diagnosing downdraft thermodynamic characteristics and subsequent boundary layer recovery of downdraft-induced low-θ_e air, they are limited by sparse measurements from dropsondes (a single profile of temperature, humidity, wind speed, and wind direction) and lack of temporal continuity (i.e., 12 h between aircraft missions). This study uses idealized simulations of mature TCs to further explore the low-level ventilation paradigm presented by Riemer et al. (2010) by investigating what factors influence the thermodynamic characteristics of downdrafts and what implications individual downdrafts have on the boundary layer and nearby updrafts. The specific objectives of the paper are to

TABLE 1. A list of the parameterizations and the domains they are applied on in both the Ideal3 and Ideal5 simulations.

Parameterization	Option	Domains
Boundary layer	Yonsei University (YSU; Noh et al. 2003; Hong et al. 2006)	All
Microphysics	WRF double-moment 6-class (WDM6; Lim and Hong 2010)	All
Radiation	Rapid Radiative Transfer Model (Iacono et al. 2008)	All
Convective	Tiedtke (Tiedtke 1989; Zhang et al. 2011)	27-km domain only
Ocean	1D Pollard–Rhines–Thompson (Pollard et al. 1973)	All

TABLE 2. A list of selected environmental variables, domain sizes, and output intervals for the Ideal3 and Ideal5 simulations.

Simulation	Domain	Domain sizes (integration time step)	Output (high temporal)	Initial vortex	Environmental winds
Ideal3	Zonal channel at 20°N ($f = 5.0 \times 10^{-5}\,s^{-1}$)	27 km: 240 × 180 (60 s) 9 km: 180 × 180 (30 s) 3 km: 360 × 360 (10 s) 1 km: 480 × 480 (5 s)	Hourly output for 8 days (2-min output from day 6 for hour 12 though hour 20)	15 m s^{-1} low-level vortex	5 m s^{-1} surface easterly flow varying sinusoidally between 850 and 200 hPa with 10 m s^{-1} shear
Ideal5	Zonal channel at 15°N ($f = 3.77 \times 10^{-5}\,s^{-1}$)	27 km: 240 × 180 (60 s) 9 km: 180 × 180 (30 s) 3 km: 360 × 360 (10 s) 1 km: 480 × 480 (5 s)	Hourly output for 8 days (2-min output from day 6 for hour 12 though hour 20)	10 m s^{-1} midlevel vortex	5 m s^{-1} surface easterly flow varying sinusoidally between 850 and 200 hPa with 5 m s^{-1} shear

1) characterize the thermodynamic characteristics of convective downdrafts in relation to TC intensity, storm structure, and storm-relative location;
2) explore, using Lagrangian parcel trajectories, the extent to which thermodynamically unfavorable air in downdrafts at different storm-relative locations enters the boundary layer and negatively influences eyewall updrafts; and
3) further quantify the role of air–sea enthalpy fluxes in the boundary layer recovery process.

2. Data and methodology

a. *Description of simulations*

This study utilizes two idealized TC simulations created using the Advanced Research version of the Weather Research and Forecasting (WRF-ARW; hereafter WRF) Model version 3.9.1.1 (Skamarock et al. 2008). The simulations were designed to produce a broad TC of category-3 (on the Saffir–Simpson scale) intensity (called Ideal3) and a compact TC of category-5 intensity (called Ideal5). Utilizing

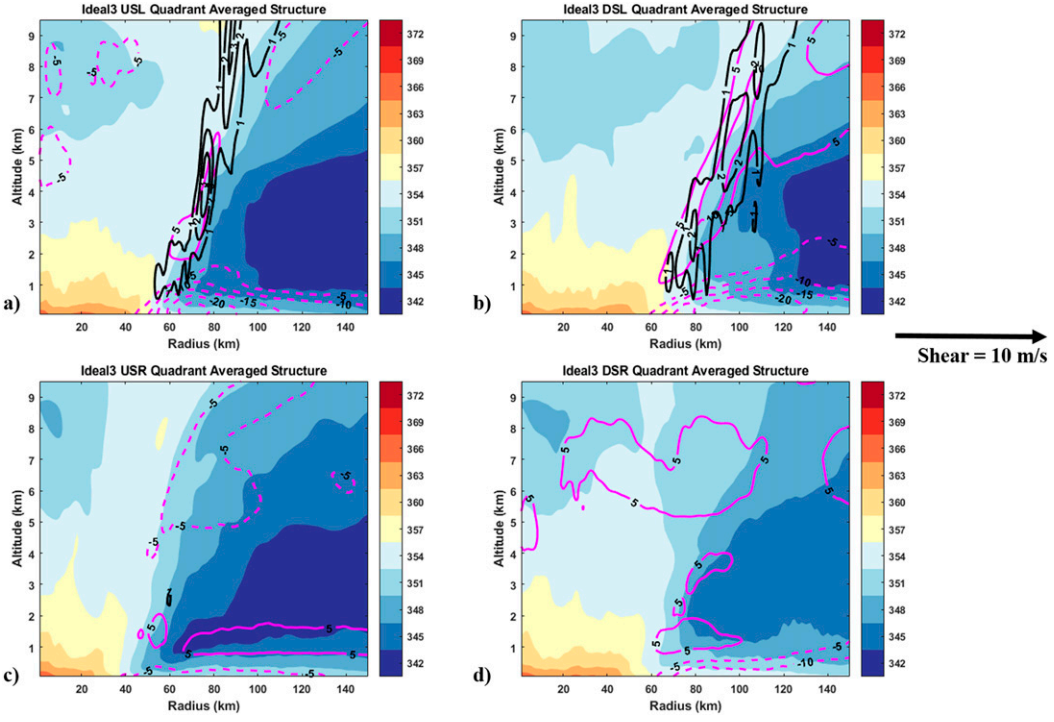

FIG. 2. Quadrant-averaged, relative to environmental wind shear, θ_e (shaded), radial wind (magenta, dashed = inflow and solid = outflow), and vertical velocity (black, dashed = downward motion and solid = upward motion) for the (a) upshear-left, (b) downshear-left, (c) upshear-right, and (d) downshear-right quadrants at hour 15 of day 6 of the Ideal3 simulation. Contour interval is 3 K for θ_e, 5 m s^{-1} for radial wind, and 1 m s^{-1} for vertical velocity. Note that there is no zero contour for radial wind and vertical velocity. The shear direction and magnitude is noted in the middle right of the figure.

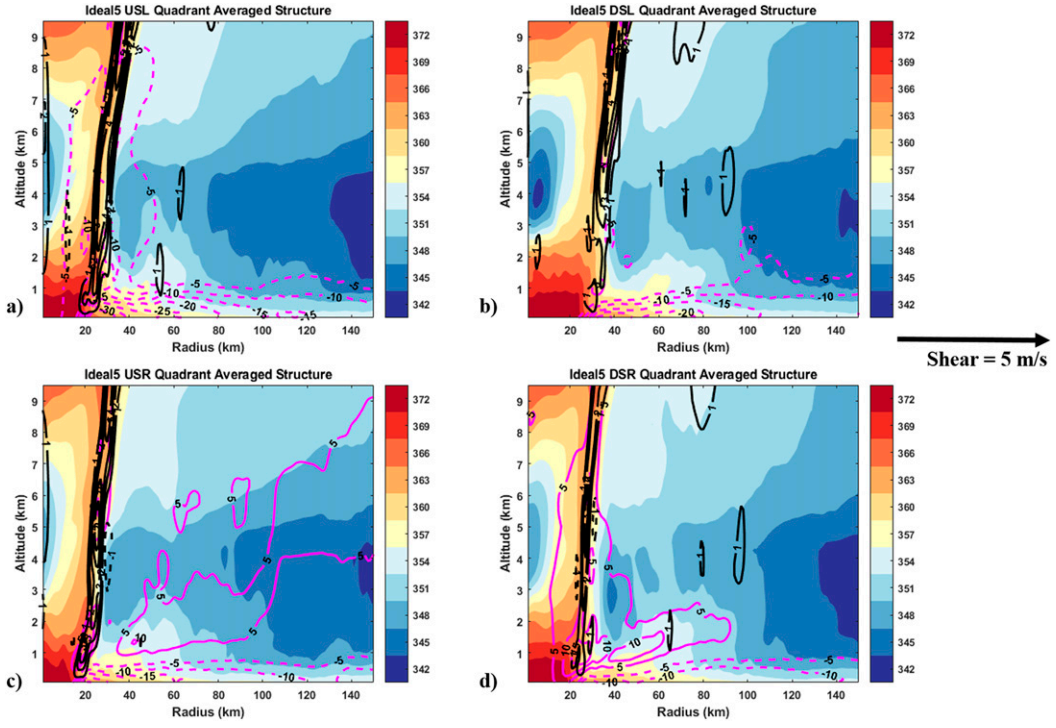

FIG. 3. As in Fig. 2, but for the Ideal5 simulation.

TCs of different size and intensity allows us to examine how storm-scale structural differences influence the effect of downdrafts on the TC boundary layer. These simulations are initially integrated for 8 days with hourly output (Fig. 1) and are updated versions of the Ideal3 and Ideal5 simulations presented in Klotz and Nolan (2019), except with WRF updated from version 3.4.1 to 3.9.1.1.

Both simulations are in large zonally periodic channels with four nested domains (innermost three are vortex-following; grid spacing in Table 2) and 60 vertical levels between the surface and 20-km altitude (lowest level is ~42 m). The physical parameterizations are the same as the Hurricane Nature Run (Nolan et al. 2013; summarized in Table 1). They are also both initialized with the Dunion (2011) moist-tropical sounding at the center of the domain. The main difference between the two simulations is the environmental setup. The temperature from the sounding is varied meridionally to balance the zonal wind shear, which is 5 m s^{-1} in Ideal5 and 10 m s^{-1} in Ideal3. The specific humidity is also varied meridionally to maintain a constant relative humidity at each height. The shear is held constant throughout the simulations through nudging of the wind, temperature, and moisture fields on the outermost domain, which also keeps the meridionally varying soundings close to their initial values (except near and within the simulated TCs). In Ideal5, the midlevel specific humidity is reduced by an additional 10% from the moist-tropical sounding to reduce the size of the resulting TC. The sea surface temperature (SST) at the center of the domain is 29°C in Ideal5 and 27°C in Ideal3, each also varying meridionally (0.22°C in Ideal5 and 0.71°C in Ideal3 in the innermost domain) to match the atmospheric temperature variations at 5-km altitude in their respective simulations. A further description of the differences in the initial conditions and domains is given in Table 2.

It is worth noting that shear magnitude, environmental sounding, and SST are different for each simulation because each is designed to produce archetypes of major hurricanes, which can also be parts of the life cycle of the same hurricane. Since the goal of this study is to assess how the differences in storm structure and intensity influence the thermodynamic properties of downdrafts and their effect on the TC boundary layer, the differences between the simulations should not be attributed to any single environmental characteristic.

b. *High-temporal-resolution output and Lagrangian trajectories*

The Ideal3 simulation undergoes steady intensification for the first 140 h of the simulation, reaching a peak intensity of ~55 m s^{-1} before gradually weakening (Fig. 1). The Ideal5 simulation undergoes steady intensification for the first 70 h, reaching an intensity of ~30 m s^{-1}, before undergoing rapid intensification and reaching peak intensity near ~70 m s^{-1} at 135 h into the simulation. The weakening after peak intensity in both simulations is due to secondary eyewall formations (not shown).

With the objective of studying the time evolution of downdrafts and using Lagrangian parcel trajectories to determine how air embedded in downdrafts influences the

storm structure, we performed model restarts to obtain output files every 2 min for 8 h. In both simulations, the high-frequency output was produced between hours 12 and 20 on day 6 (hours 132–140 of the simulations; outlined in Fig. 1) which was near peak intensity for each simulation. Unfortunately, the numerical evolutions of the restart simulations did not exactly match the originals, which is a known issue with the WRF Model when using vortex-following nested grids. However, in both cases the simulated TCs remained very close to the intensity and structure of the original TCs over the relatively short 8-h integration times (not shown). Unless noted, all of the trajectories and analysis in this manuscript are from the restart simulations with high-frequency output.

Before starting the parcel trajectories, each model output time was mapped to the same latitude and longitude grid to eliminate the movement of the vortex-following nests. Following Onderlinde and Nolan (2016), the trajectories are created using the predictor–corrector (also known as modified Euler) methodology which updates (or ''corrects'') a parcel's location and heading between each iterative step. Once a parcel is initiated, a local grid is created between the initial output time and the next model output 2 min later and includes all vertical levels, but is 20 km in each horizontal direction from the parcel's initial location. The local grid is interpolated in both space and time based on the number of corrector time steps. In this study, the corrector time step is 3 s, meaning that between the 2-min output files there were 40 interpolated fields.

The wind components are interpolated to the parcel's location and used as a predictor for the parcel's future location. Once the parcel is integrated forward 3 s to the predicted location, three new velocity components are computed based on the parcel's predicted latitude, longitude, and altitude. The velocity components at the predicted location are averaged with the initial velocity components to ''correct'' the trajectory. The averaged velocity components are then used for actually integrating the parcel forward 3 s from its initial location. Thus, for every 3 s of the trajectories, the parcel is integrated forward based on the initial (predictor) velocity field, the predictor velocity is corrected based on averaging the predictor and final velocity components from the 3-s integration, and the corrected velocity is used to actually update the parcel's latitude, longitude, and altitude from its initial location. Along the trajectory, thermodynamic data are saved using the same interpolation mechanism.

Two sets of trajectories are computed in this study: those initiated directly into downdrafts, and those initiated in an annulus around the storm. For trajectories initiated in downdrafts, parcels are initiated at locations at a fixed azimuth angle and inside the $-1\,\mathrm{m\,s^{-1}}$ vertical velocity contour. The number of trajectories per downdraft depended on the size of the downdraft, but varied between 41 and 122. With the goal of using these trajectories to diagnose how downdraft characteristics (e.g., storm-relative location, altitude, location relative to closest updraft) are related to their effect on the boundary layer, those

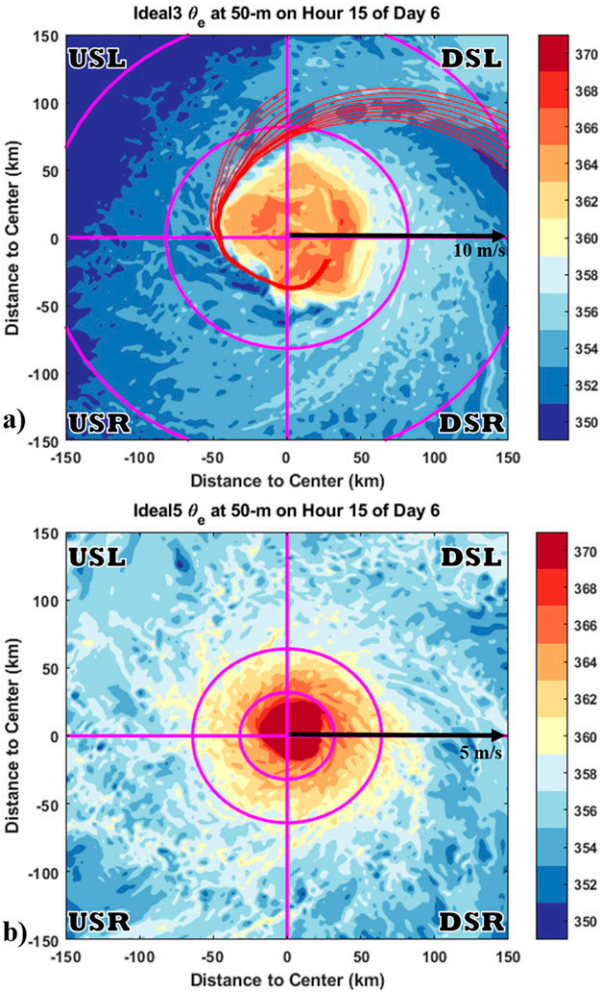

FIG. 4. (a) The 50-m-altitude θ_e at hour 15 of day 6 of the Ideal3 simulation. The black arrow represents the shear vector while the shear-relative quadrants are outlined. The magenta range rings represent 1 × RMW and 2 × RMW at 2-km altitude. (b) As in (a), but for the Ideal5 simulation. An inflow trajectory is outlined in (a) with red streamlines. The contour interval in both plots is 2 K.

described in the manuscript demonstrate properties that were observed in many other downdrafts with similar characteristics.

The second set of trajectories were initiated for parcels in an annulus on hour 15 of day 6 (same time as the downdrafts; described in section 3a) of the Ideal3 simulation, and are used to objectively verify the effects of individual downdrafts found in Ideal3. The annulus of parcels ranges between 62- and 122-km radius [0.75 and 2 times the 2-km radius of maximum wind (RMW) speed] and between 500-m and 6-km altitude. Parcels are initialized with a grid spacing of 1 km (radially) and 2° (azimuthally), leading to 206 460 parcels. All the trajectories in the annulus were initially integrated forward for 1 h. The parcels identified as entering a convective downdraft during the first hour, defined as being below 5-km

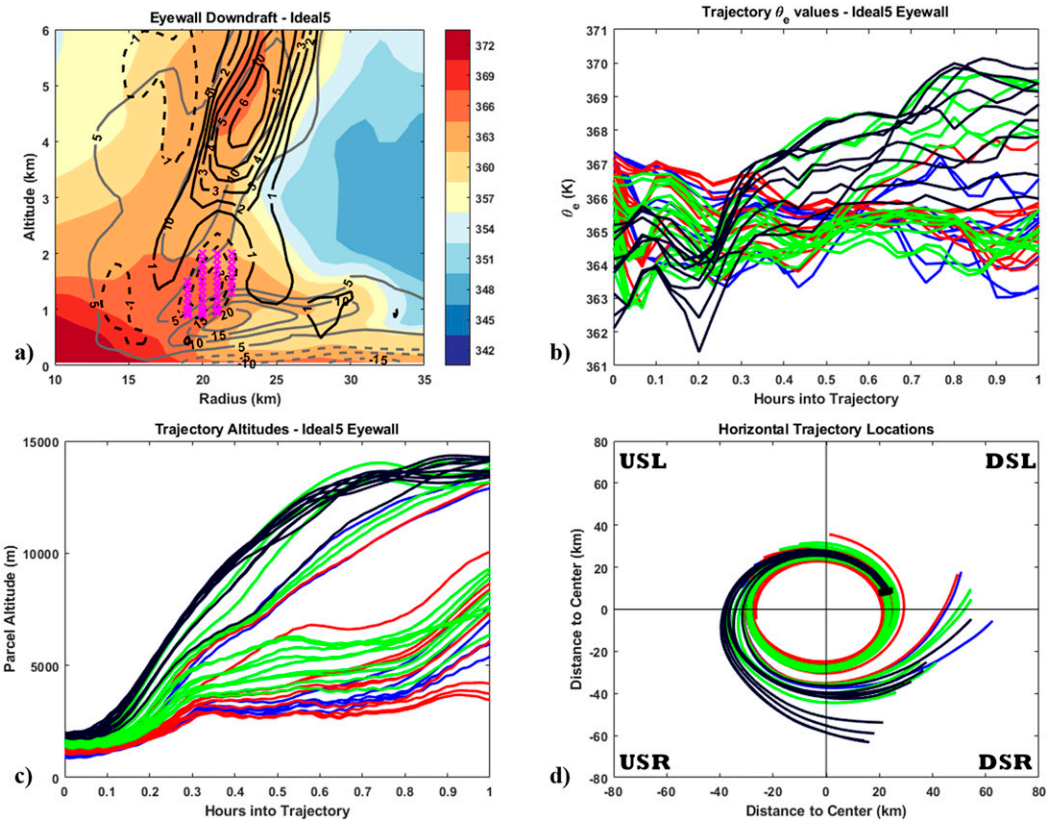

FIG. 5. (a) Radial cross section of a convective downdraft underneath the eyewall in Ideal5, (b)–(d) 1-h trajectories for 41 parcels of θ_e, altitude, and storm-relative horizontal location, for parcels initiated in the convective downdraft. The color of parcels is based on initial altitude (h_0) with blue: $h_0 \leq 1000$ m; red: $1000 < h_0 \leq 1350$ m; green: $1350 < h_0 \leq 1700$ m; and black: $h_0 > 1700$ m. In (a), initial parcel locations are noted by magenta × symbols while the contour interval is 3 K for θ_e (shaded), 5 m s^{-1} for radial wind (gray, dashed = inflow and solid = outflow), and 1 m s^{-1} for vertical velocity (black, dashed = downward motion and solid = upward motion). Note that there is no zero contour for radial wind and vertical velocity. In (d), the shear-relative quadrants are outlined.

altitude and having a -1 m s^{-1} vertical velocity for over 5 continuous minutes (9095 trajectories), were integrated forward for a second hour.

3. Results

a. Generalized storm structure

All the downdrafts identified in this study occur between hours 15 and 16 on day 6 (3 h into restart) of the simulations to allow time for forward and backward parcel trajectories. Since convective downdrafts typically form and decay within 10–20 min, many of the downdraft signatures were most pronounced at different times of each hour. For brevity, hereafter the downdrafts are only referred to by the hour they occur. The quadrant-averaged radius–height storm structure relative to environmental wind shear on day 6, hour 15 for Ideal3 and Ideal5 are shown in Figs. 2 and 3, respectively. In Ideal3, the strongest eyewall vertical velocities are left of shear, with quadrant-averaged vertical velocities exceeding 2–3 m s^{-1} in the eyewall region. The left-of-shear quadrants also have the strongest and deepest inflow layers, with inward radial wind speeds exceeding 20 m s^{-1}. Outflow layers are present above the inflow layer at ~1-km altitude in the right-of-shear quadrants. Below 2-km altitude of the eyewall region (60–80-km radius), the θ_e (calculated using the method of Bolton 1980) is highest in the downshear-left (DSL) quadrant (between 350 and 359 K with a mean of 355.2 K) and lowest in the upshear-right (USR) quadrant (between 342 and 353 K, with a mean of 346.5 K).

The storm structure in the Ideal5 simulation (Fig. 3) is more symmetric than in Ideal3. Quadrant-averaged vertical velocities in the eyewall region exceed 4 m s^{-1} in all quadrants, and each quadrant contains inflow throughout the lowest 1 km. There is an outflow layer immediately above the inflow layer in the DSR quadrant. Unsurprisingly, with higher SSTs across the domain, the θ_e values in the boundary layer of Ideal5 are greater than those in Ideal3. Between 20- and 80-km radius of all quadrants, a region

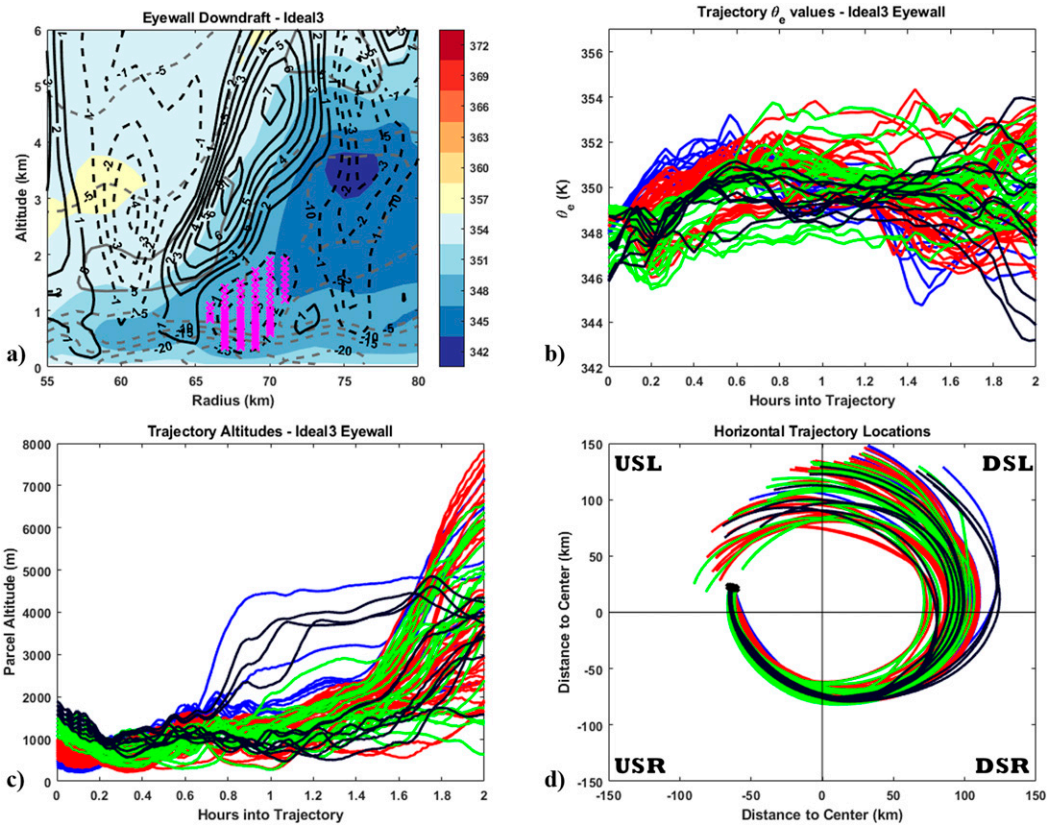

FIG. 6. As in Fig. 5, but for 88 parcel trajectories integrated over 2 h that were initially in a downdraft underneath the eyewall in Ideal3. The color of parcels is based on initial altitude (h_0) with blue: $h_0 \leq 500$ m; red: $500 < h_0 \leq 1000$ m; green: $1000 < h_0 \leq 1500$ m; and black: $h_0 > 1500$ m.

between 1- and 2-km altitude is characterized by quadrant-averaged θ_e values between 350 and 357 K, which are relatively high values for those altitudes and are only slightly reduced compared to the inflow layer below. This layer of higher-θ_e air results in the vertical confinement of the region of low midtropospheric θ_e air in Ideal 5 (between 2- and 5-km altitude), which plays a critical role in determining the effects of downdrafts on the boundary layer thermodynamic structure [discussed in section 3b(2)].

At 50-m altitude, the lowest level to which we can interpolate, the θ_e outside of the eye in Ideal5 (Fig. 4b) is more azimuthally uniform than Ideal3 (Fig. 4a). In Ideal3, there are localized areas of relatively low-θ_e air (i.e., <350 K) along an inflow trajectory from the DSR to USL quadrant (indicated by red streamlines in Fig. 4a). These areas of low-θ_e air reach inward to ~40-km radius in the USR quadrant, mixing with air in the low-level eye. Additionally, there is a broader-scale distribution of low-θ_e air in the USL and USR quadrants from ~100- to 200-km radius (only shown to 150 km). The source of these low-entropy regions is discussed throughout section 3b. In contrast to the distribution in Ideal3, the 50-m θ_e in Ideal5 shows relatively small variations and no identifiable inflow trajectory of low-θ_e air that reaches the eyewall region. Within 2 times the RMW, the θ_e is uniformly above 357 K.

b. *Development and evolution of downdrafts*

1) DOWNDRAFTS IN THE EYEWALL REGION

The thermodynamic effects of convective downdrafts underneath the eyewall depend on storm structure. A radial cross section of the eyewall in the DSL quadrant of the Ideal5 simulation (Fig. 5a) shows θ_e values exceeding 360 K from the surface layer to above 6-km altitude within the eyewall. The presence of outflow (solid gray contours) inside the eyewall below 2-km altitude indicates that the high-θ_e air in the eyewall updraft originated in (or at least passed through) the low-level eye which is often referred to as a reservoir of high-θ_e air (i.e., Cram et al. 2007; Barnes and Fuentes 2010; Dolling and Barnes 2012). A downdraft with peak downward vertical velocities greater than 3 m s^{-1} (maximized at 1.5-km altitude) is in the region of low-level outflow. In the Ideal5 simulation, this signature was observed in many eyewall downdrafts, especially downshear. Forward trajectories from 41 parcels that originate in this downdraft (Figs. 5b–d) show that the θ_e of parcels generally decreased by ~2 K over the first 0.1 h after being advected just outside the eyewall (and the downdraft) by outflow. However, the parcels quickly recovered and by 0.15 h most were back to their original θ_e values. By 0.5 h, parcels already traveled

half a circumnavigation of the eyewall, with most parcels above 5 km, and some above 10-km altitude. The parcels that were above 10-km altitude tended to be those that were initiated above 1700 m (the black lines). With all parcels that enter the eyewall from the downdraft having θ_e values above 361 K (Fig. 5b), and air originally within the eyewall having mean θ_e value of 359.4 K (range of 352.5–365.9 K) for all grid points with vertical velocities greater than 5 m s^{-1}, this type of downdraft presents no negative thermodynamic influence to the eyewall or boundary layer.

In contrast to the eyewall region downdraft in Ideal5, a downdraft in the eyewall region of the USL quadrant in Ideal3 is characterized by θ_e values between 346 and 349 K (Figs. 6a,b). This downdraft presents a potentially negative influence on the boundary layer entropy and eyewall updraft (defined throughout this manuscript as leading to a θ_e reduction of 1 K or greater) which has θ_e values ranging between 345.8 and 366.1 K for grid points within the 4 m s^{-1} contour (Fig. 6a). In Ideal3, the largest horizontal gradient of θ_e in the midlevels (i.e., 2–5-km altitude) is near the outer edge of the eyewall. Thus, any downdraft radially outward of the eyewall can transport low entropy air to the inflow layer where, because of its proximity, can quickly move radially inward and enter the base of eyewall updrafts.

Forward trajectories from 88 parcels in the eyewall downdraft of Ideal3 show two distinct pathways (Figs. 6b–d). Parcels initiated below 1000-m altitude (blue and red lines) generally remained in the downdraft for ~0.1 h, before increasing in altitude to between 750 and 1250 m by the end of the first hour of the trajectory. Parcels initiated above 1000 m (green and black lines) generally had initially lower θ_e values (~346–348 K compared to 348–349 K for those below), and remained in the downdraft for ~0.4 h. All the parcels from this downdraft traveled to the DSR quadrant by the end of the first hour integration and none of them ascended above 5.0-km altitude. Subjective forward tracking of the minimum θ_e at 400-m altitude confirms that air within the downdraft traveled radially inward below the base of eyewall updrafts (not shown). At ~1.2 h into the trajectories, a cluster of parcels entered eyewall updrafts and, by 1.6 h, those parcels traveled above 3 km and had a mean θ_e of 349.5 K (ranging from 347.6 to 350.9 K). This is a significant reduction to the initial eyewall updraft, which had mean θ_e of 353.0 and 354.7 K for grid points with positive vertical velocity values above 2 and 4 m s^{-1}, respectively (Fig. 6a). Of the parcels that entered the updraft, 81% experienced vertical velocity values greater than 2 m s^{-1} during this time, meaning they were not only sampling the updraft periphery and that this is a fair comparison with initial eyewall θ_e values. Thus, in Ideal3, parcels initially in the downdraft were not able to fully recover and had a 4–7-K deficit in θ_e compared to initial eyewall values (mean deficit of 5.2 K compared to air within to 4 m s^{-1} upward vertical velocity contour in the initial updraft) even though they initially passed underneath and radially inward of the eyewall.

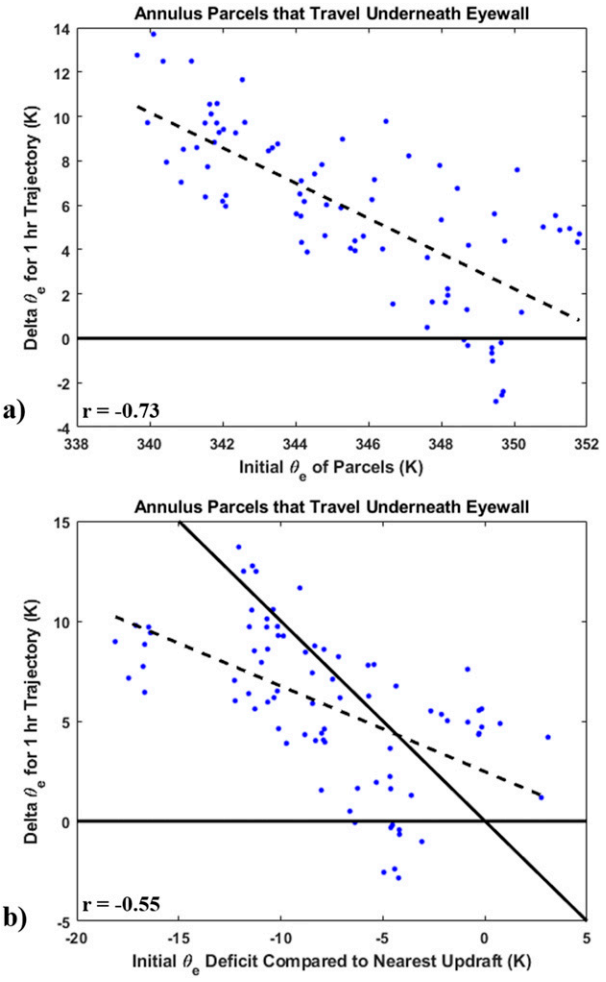

FIG. 7. Statistics for parcels that enter a downdraft radially outward of the RMW and travel radially inward of 0.8 × RMW below the eyewall (1500-m altitude) of the Ideal3 simulation. (a) Comparison of the initial θ_e of parcels as they enter the downdraft with the change in θ_e over a 1-h trajectory. (b) Comparison of the initial θ_e deficit of parcels (θ_e value at peak upward velocity of closest updraft − initial θ_e of parcel) with the change in parcel θ_e value over a 1-h trajectory. In both panels the zero change in θ_e is outlined, the black dashed line is the line of best fit, and the r value in the bottom right of each panel is the Pearson correlation coefficient. In (b) a 1:1 line is also outlined in solid black.

Unlike the eyewall downdraft in Ideal5, the parcels from the downdraft in Fig. 6 were too far away from the storm center to mix with the reservoir of high-θ_e values in the eye. Given the broad circulation, this was found to be the case in many eyewall downdraft trajectories sections in Ideal3 (not shown) and in the trajectories initiated in the annulus (Fig. 7). Out of the 9095 trajectories that entered downdrafts, 81 followed a similar trajectory to the downdraft described in Fig. 6 by starting outside the RMW, traveling below 1500-m altitude (the approximate base of eyewall updrafts), and reaching inside of 0.8 times the RMW. For

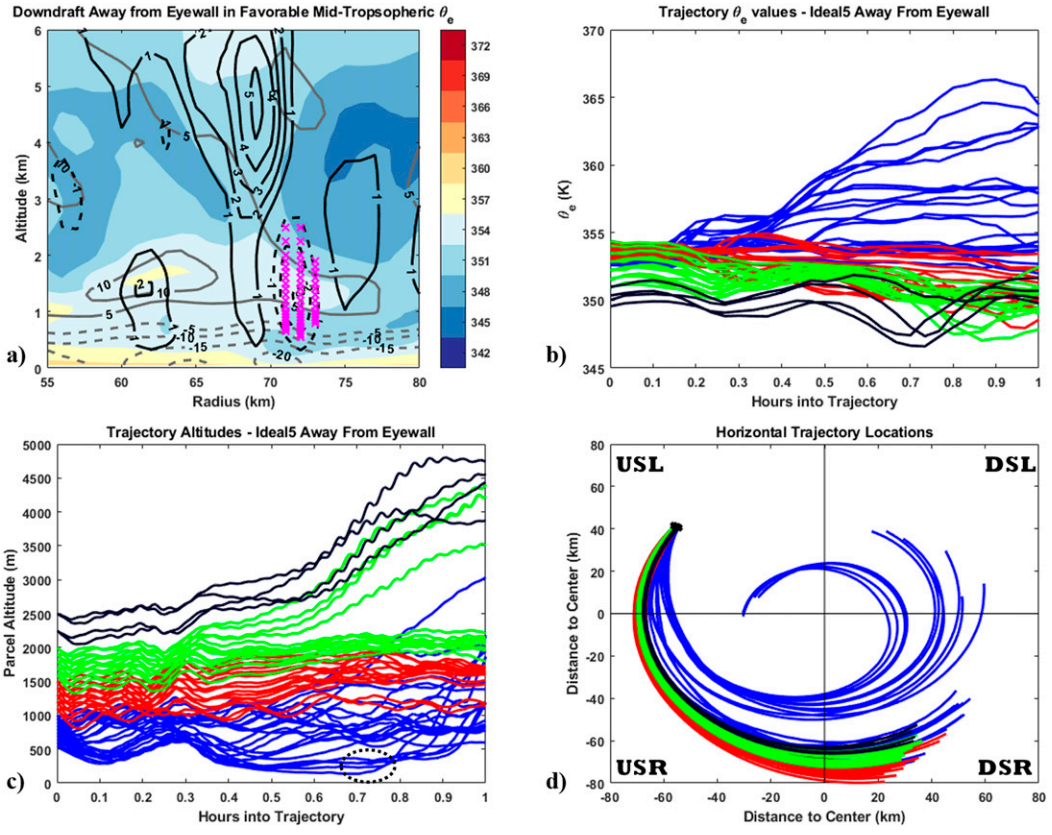

FIG. 8. As in Fig. 5, but for 56 parcel trajectories integrated over 1 h that were initially in a convective downdraft characterized by the favorable midtropospheric thermodynamic environment in Ideal5. The color of parcels is based on initial altitude (h_0) with blue: $h_0 \leq 1000$ m; red: $1000 < h_0 \leq 1500$ m; green: $1500 < h_0 \leq 2000$ m; and black: $h_0 > 2000$ m. The circled parcels in (c) are the ones that enter eyewall updrafts later in the trajectory integration.

each of those parcels, we identified the strongest updraft within 15-km radius and at the same azimuth as the downdraft (for consistency with the cross sections) at the time they entered a downdraft. One hour after the parcels entered a downdraft and traveled radially inwards of the eyewall, 72 of the 81 trajectories (89%) demonstrated increased θ_e values (Fig. 7a). The change in θ_e was negatively correlated ($r = -0.73$) with the initial parcel θ_e values. This is consistent with the results presented in Cram et al. (2007), which showed that many trajectories initiated in the inflow layer travel inwards, underneath the eyewall, and then increase their θ_e values in the eye before entraining into eyewall updrafts. However, after the 1 h of integration, 55 of the trajectories (68%) still had θ_e values lower than those initially in the updraft (Fig. 7b; mean final θ_e deficit is 2.0 K), signifying that a majority of parcels did not increase their θ_e values significantly enough to avoid being thermodynamically unfavorable to eyewall updrafts.

2) FAVORABLE CONVECTIVE DOWNDRAFTS AWAY FROM EYEWALL

In Ideal5, there is a layer of relatively high-θ_e air in all quadrants approximately between 1- and 2-km altitude and between 40- and 80-km radius (Fig. 3). Though not necessarily at the same altitude, the increased θ_e above the near-surface layer is similar to what was observed in Hurricanes Bonnie (1998), Mitch (1998), and Humberto (2001) from individual dropsondes released from the NOAA P-3 aircraft (Barnes 2008) and in Hurricane Michael (2018) from dropsondes released by the NOAA G-IV aircraft (Wadler et al. 2021). In Barnes (2008), the increase in midlevel θ_e was attributed to outflow above the inflow layer that originated in the eyewall region (what Barnes called differential advection). With an outflow layer above the boundary layer inflow previously identified in composite studies of TC structure in shear (Reasor et al. 2013; Zhang et al. 2013; DeHart et al. 2014) and in numerical simulations (Zhang et al. 2000, 2001; Nolan et al. 2009, 2013; Moon and Nolan 2015; Li and Dai 2020), Wadler et al. (2021) showed how the enhanced secondary circulation in the downshear quadrants can lead to high midlevel θ_e values throughout that region. By transporting high-θ_e air away from the eyewall, this process can lead to an area of convective stability in the upper boundary layer which shields the boundary layer from low-θ_e midtropospheric air and allows for rapid energy

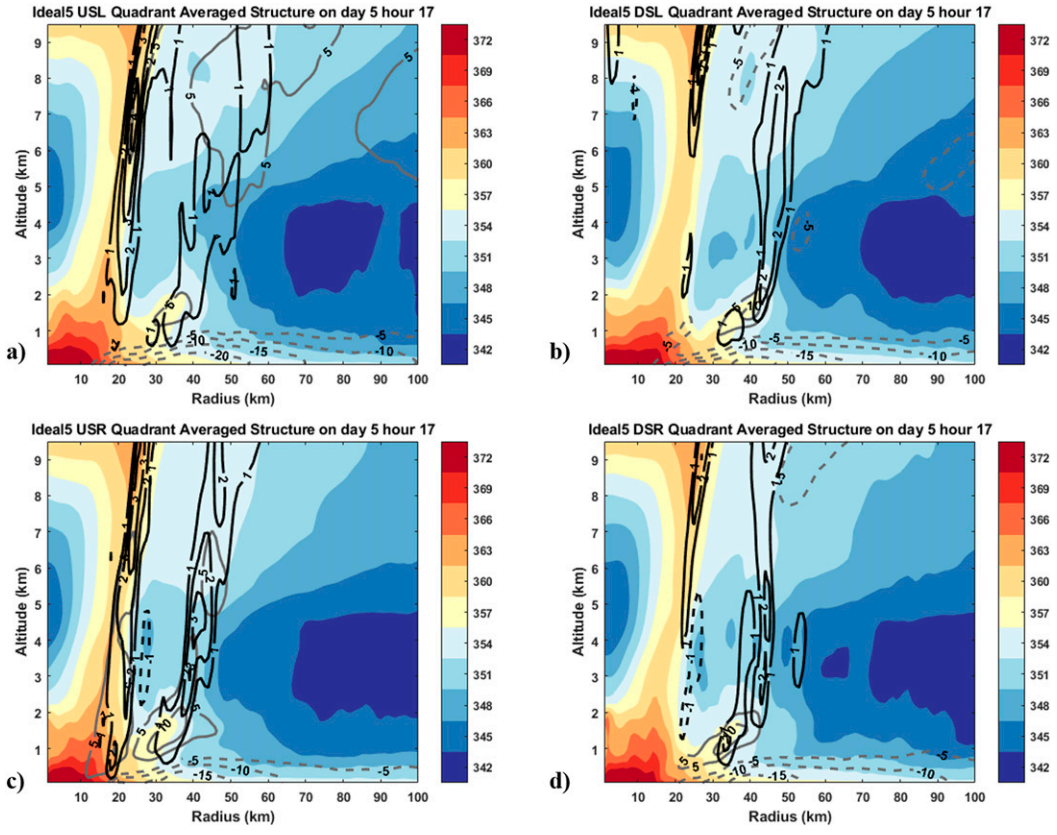

FIG. 9. As in Fig. 3, but for hour 17 on day 5.

increases in the inflow layer due to air–sea enthalpy fluxes (Hawkins and Imbembo 1976; Rotunno and Emanuel 1987; Barnes and Powell 1995; Wang et al. 2001; Wroe and Barnes 2003).

A cross section through a convective downdraft (Fig. 8a) in the USL quadrant of Ideal5 reveals how this high-θ_e layer reduces the amount of θ_e recovery needed for downdrafts. The background θ_e in the outflow layer (average between 60–70-km radius and between 1- and 2-km altitude) is 354.9 K, which is virtually the same as the average θ_e of 354.8 K in the layer below (averaged between 60- and 70-km radius and between 0.1- and 1-km altitude). Forward trajectories from 56 parcels that originate in the downdraft (with average initial θ_e of 352.8 K) reveal that by the end of the first hour, 47 of the parcels have θ_e values between 350 and 355 K and remain below 2500-m altitude. However, a parcel originally in this downdraft descended to as low as 145-m altitude at 0.7 h. For the five parcels that remain below 300-m altitude between 0.5 and 0.7 h (circled near 0.7 h in Fig. 8c), the average increase in θ_e over that time is 2.50 K (12.5 K h^{-1} heating rate). These parcels were initiated in the high-θ_e region near the top of the inflow layer, spiraled inward (Fig. 8d), and reached eyewall updrafts by 1.1 h into the trajectories with θ_e values of between 363 and 367 K (only up to 1 h shown), comparable to values in the eyewall shown in Figs. 3 and 5.

Since the amount of θ_e recovery needed to reach eyewall values was reduced because these parcels were initiated with relatively high-θ_e values, the high-θ_e region above the boundary layer leads to an easier and more efficient pathway for recovery. Similar pathways were found in downdrafts initiated in the high-θ_e layer from other quadrants (not shown). In addition to requiring less recovery due to initially high-θ_e values, the enhanced convective stability in the high-θ_e region also led to a reduction of the vertical displacement of parcels. The mean vertical displacement of parcels while they were in the downdraft in Fig. 8, and in another downdraft initially in the high-θ_e layer of the DSL quadrant (not shown) was 202.3 and 125.0 m, respectively. In contrast, the vertical displacement of two midlevel downdrafts in Ideal3 [discussed in section 3b(3)] are 1103.0 and 540.6 m (despite similar initial mean altitudes of the parcels). The greater average vertical distance that parcels travel when not initiated in a layer of high θ_e highlights how the increased convective stability of that layer, or the reduced negative buoyancy of parcels, can reduce downdraft intrusions into the inflow layer.

Since the interesting aspect of the downdraft in Fig. 8 is the region of relatively high-θ_e values between 1- and 2-km altitude which creates a ''thermodynamic shield'' against the reduction of inflow-layer θ_e, its origin is explored further. Quadrant-averaged cross sections were created

using the hourly output from the full 8-day simulation (i.e., not the restart simulation). The first time this high-θ_e air emerges is hour 9 on day 5 (not shown). At this time, the high-θ_e air is coincident with outflow and developing updrafts between 20- and 40-km radius at ~1.5-km altitude in all quadrants except the USL. By hour 17 on day 5, a secondary eyewall feature emerges (Fig. 9). Outflow between 1- and 2-km altitude in all quadrants connects the low-level eye to the secondary eyewall and is characterized by higher θ_e values. Thus, the high-θ_e layer is a result of outflow from the high entropy eye–eyewall region (and not due to a lack of downdrafts in this region). By the time of the downdrafts analyzed in this study (hour 15 on day 6), the secondary eyewall contracted to 20-km radius (Fig. 3).

To further understand the evolution of the high-θ_e layer, backward trajectories were initiated at 45° azimuth into all quadrants between 1- and 2-km altitude and between 40- and 90-km radius on hour 15 of day 6 and integrated backward for 2 h (Fig. 10). After the 2-h backward integration, 404 out of 484 parcels had θ_e values between 345 and 355 K (compared to initially 385 out of 484 parcels) and 436 parcels remained below 3000-m altitude (not shown). Additionally, while some parcels move away from this region and into the inflow layer, a majority of parcels maintain a consistent storm-relative radial location (Fig. 10a; 245 parcels have a final radius within 25-km radius of their initial radius), similar values of θ_e (Fig. 10b), and altitude (Fig. 10c). The difference in average parcel radial location and θ_e between the initial and final time of the integration decreases with increasing initial altitude. Parcels initially between 1500 and 1750 m (1750 and 2000 m) have a mean radial displacement of 20.8 km (11.1 km) and θ_e change of −1.68 K (−0.98 K) over the 2-h backward trajectory, indicating that many parcels in this region are following nearly circular trajectories. With little radial and vertical motions over the area of high θ_e between 1- and 2-km altitude and between 20- and 40-km radius at this time, the thermodynamically favorable air remains in mostly circular motion which limits the potential for any negative influences that can reduce θ_e values (i.e., advection, negative turbulent fluxes, and radiative divergence).

3) Unfavorable convective downdrafts away from eyewall

While the layer of high-θ_e air outside the eyewall in Ideal5 can prevent negative thermodynamic influences to the inflow layer, this layer did not appear in Ideal3 and multiple convective downdrafts in that simulation were identified transporting low-θ_e air toward the boundary layer. For example, a convective downdraft with a peak downward vertical velocity of 4 m s^{-1} at 1-km altitude is underneath an updraft with a peak upward vertical velocity of 3 m s^{-1} at 3-km altitude (Fig. 11a). In this downdraft, the −1 m s^{-1} contour extends downward to 200-m altitude and low-θ_e air (<345 K) appears in the near-surface layer. Trajectories from 102 parcels that originate in this downdraft show that

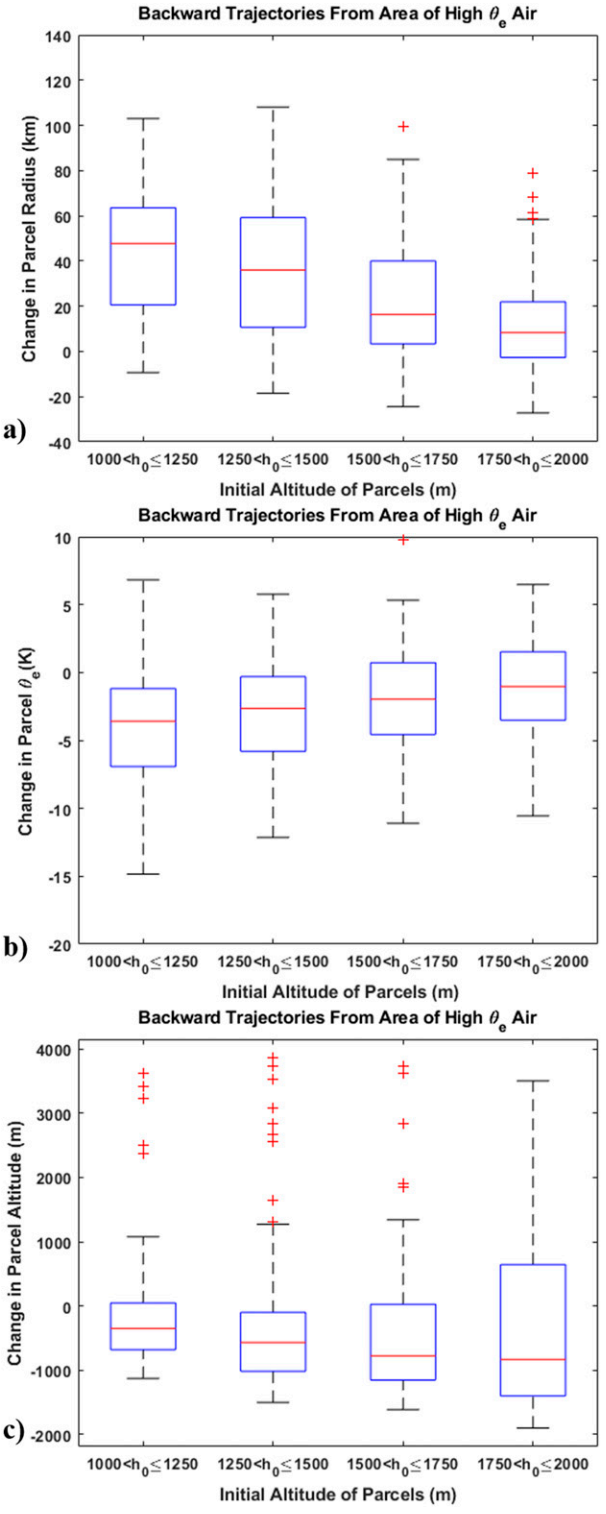

FIG. 10. Boxplots for the 2-h backward trajectories of change in parcel (a) radius, (b) θ_e, and (c) altitude for 121 parcels initiated in each quadrant between 1- and 2-km altitude of the Ideal5 simulation. Each panel is broken up by the initial parcel altitude.

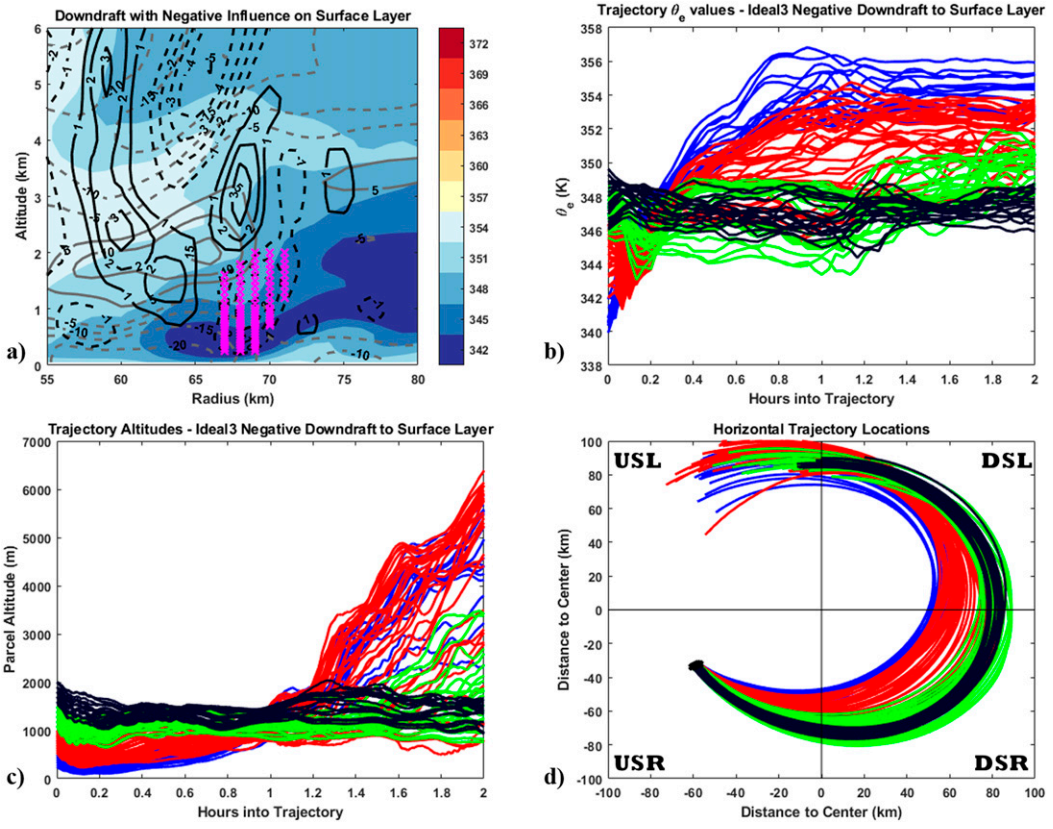

FIG. 11. As in Fig. 5, but for 102 parcel trajectories integrated over 2 h that were initially in a low-level downdraft in Ideal3. The color of parcels is based on initial altitude (h_0) with blue: $h_0 \leq 500$ m; red: $500 < h_0 \leq 1000$ m; green: $1000 < h_0 \leq 1500$ m; and black: $h_0 > 1500$ m.

most of them stayed in the downdraft for 0.1 h, with 7 parcels descending as low as 150-m altitude (Fig. 11c). After that, parcels underwent significant boundary layer recovery (parcels that recovered were generally below 800 m for the first 0.8 h) with θ_e values increasing from ~340–344 K to 352–357 K over the first hour of the trajectory (Fig. 11b). For parcels initialized below 500 m (blue lines), the average increase in θ_e between 0.2 and 0.4 h (average parcel altitude during that time is 300.6 m) is 2.96 K (14.8 K h^{-1} heating rate).

For the low-level (i.e., below 1000 m) parcels, the boundary layer recovery is likely due to a combination of air–sea enthalpy fluxes and turbulent mixing. The results are consistent with previous observational studies of Molinari et al. (2013), Zhang et al. (2017), Wadler et al. (2018a), and Rudzin et al. (2020) and the modeling study of Onderlinde and Nolan (2016), which all showed that the enthalpy fluxes provide enough energy for the boundary layer to recover from downdrafts. The recovery is significant because at ~1 h into the trajectories, the parcels with initially low-θ_e values near the sea surface ascended into updrafts at 55–60-km radius and rose throughout the second hour toward 5–6-km altitude. Because of the recovery, these parcels reached θ_e values similar to that in eyewall updrafts (e.g., Fig. 6) and do not pose a negative thermodynamic influence for the updraft. Note that the parcels initiated between 1- and 2-km altitude (black and green lines) started above the inflow layer maintained a similar θ_e and altitude throughout the entire trajectory.

With the significant boundary layer recovery that occurs for parcels near the surface, it appears that the downdrafts with the most negative influence for eyewall updrafts are in the midlevels (i.e., above the top of the inflow layer). One example of a midlevel downdraft that negatively influences an updraft is shown in Fig. 12. The peak downward vertical velocity is at 1.9-km altitude which is underneath and 5 km radially outward of a strong updraft greater than 8 m s^{-1}. Interestingly, even though the -1 m s^{-1} contour extends downward to 600-m altitude, the low-θ_e air from the mid-troposphere does not reach the near-surface layer (the contours of θ_e are relatively flat below 800 m).

This midlevel downdraft is in a deep inflow layer, and forward trajectories from 122 parcels initialized in the downdraft indicate that parcels travel radially inward toward the updraft (77 parcels enter the updraft by 0.1 h). By 0.3 h, parcels ascend upward to 5-km altitude, but then generally descend back toward 3 km. While there is an initial increase in θ_e for parcels initialized below 1500 m before their ascent at 0.1 h, the maximum increase of θ_e is

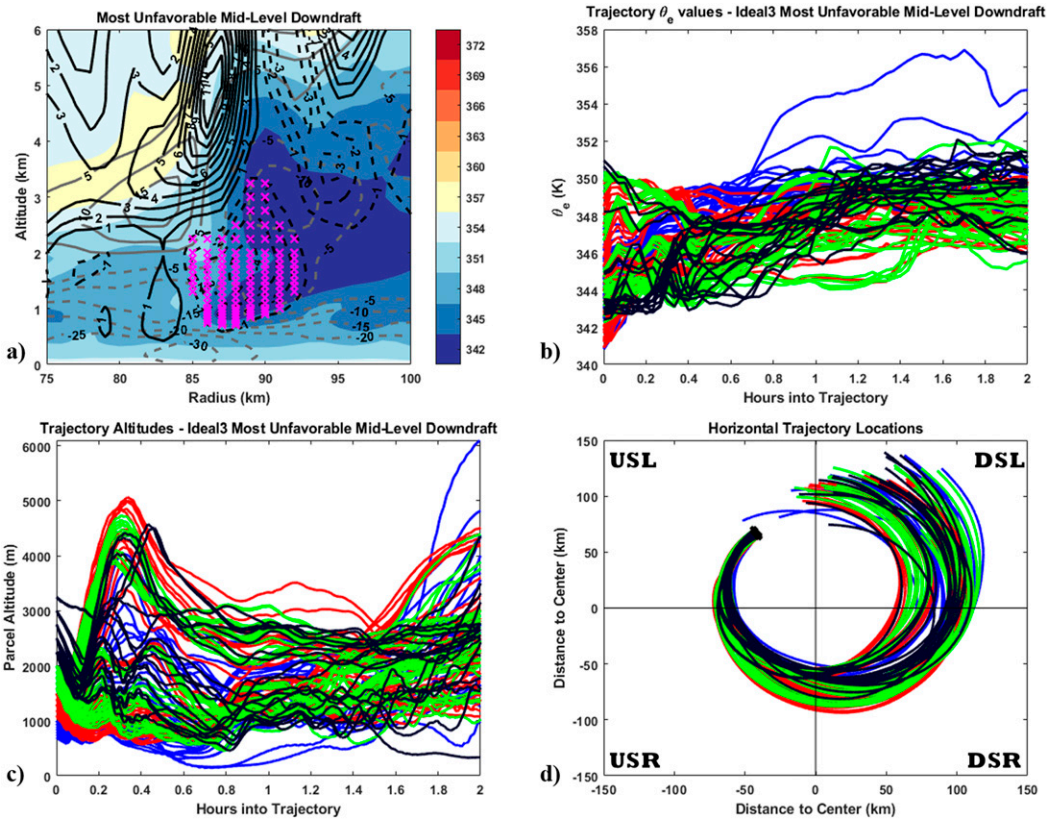

FIG. 12. As in Fig. 5, but for 122 parcel trajectories integrated over 2 h that were initially in a midlevel downdraft in Ideal3. The color of parcels is based on initial altitude (h_0) with blue: $500 \leq h_0 \leq 1000$ m; red: $1000 < h_0 \leq 1500$ m; green: $1500 < h_0 \leq 2000$ m; and black: $h_0 > 2000$ m.

3.5 K because of the low amount of time the parcels were below 1 km. With the short time for recovery and the larger distance from the sea surface compared to parcels initiated in the low-level downdraft in Fig. 11, the mean θ_e for parcels that are embedded in the updraft at 0.2 h is 346.1 K. This is a significant reduction in θ_e for the updraft, as the mean θ_e for all grid points with upward vertical velocities greater than $4\,\mathrm{m\,s^{-1}}$ in Fig. 12a is 354.3 K. This downdraft has a more significant decrease in θ_e compared to the downdraft identified in the eyewall region [section 3b(1)]. In that case the mean θ_e for parcels that originated in the downdraft and then entered eyewall updrafts (Fig. 6) was 349.5 K as compared to initial 354.7-K eyewall updraft values (mean 5.2-K deficit) for all grid points with upward vertical velocities greater than $4\,\mathrm{m\,s^{-1}}$.

To emphasize the unfavorable nature of the downdraft further, the minimum of θ_e within the midlevel downdraft is subjectively tracked forward at 2-km altitude in time using the 2 min outputs (Fig. 13). Six minutes after parcels were initiated (0.10 h), the low-θ_e air from the downdraft traveled into the inflow layer and began to enter the radially inward updraft (arrow in Fig. 13a). This is coincident with the time many parcels entered the updraft (Fig. 12c). By 14 min (0.23 h) after parcels were initiated, low-θ_e air has traveled to 4-km altitude, near the peak of updraft vertical velocities. Subsequently, this updraft core weakens significantly (not shown) and the parcels start descending (Fig. 12c).

While the thermodynamic impact of downdrafts is maximized near the top of the inflow layer because surface enthalpy fluxes cannot contribute as much to recovery of θ_e, some downdrafts are too far away from an updraft to have a negative influence. Figure 14 shows a midlevel downdraft with a peak downward vertical velocity of $4\,\mathrm{m\,s^{-1}}$ at ~2.2-km altitude, near the midtropospheric minimum of θ_e (Fig. 14a). The downdraft is underneath a strong updraft with a peak vertical velocity maximized above 6-km altitude. Trajectories from 108 parcels that originate in the downdraft show general descent for the first 0.2 h (Fig. 14c). By 0.4 h, 86 parcels remain near 1.0-km altitude, with the lowest parcel descending to 650 m. From 0.4 to 2 h, all parcels maintain a relatively constant altitude. While there was some recovery (Fig. 14b), especially for the parcels with an original θ_e below 340 K, none of the parcels obtained a θ_e value above 352.5 K, and the average increase in θ_e over the first hour for all parcels is only 2.51 K. While this air would certainly lead to a reduction of θ_e values in updrafts, no parcels descended low enough to enter the inflow layer (the average change in radius for parcels is 5.56 km over the first hour) and, unlike the downdraft in Fig. 12

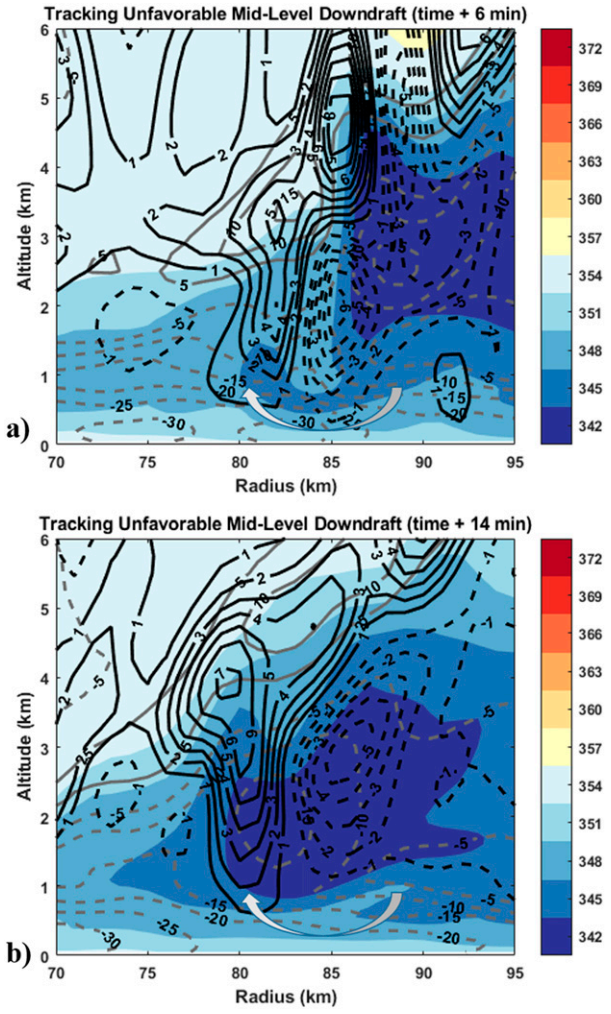

FIG. 13. Radial cross sections from forward tracking for (a) 6 and (b) 14 min, the midlevel downdraft in Ideal3. In both panels, the arrow indicates how low-θ_e air enters the updraft. In both panels, the contour interval is 3 K for θ_e (shaded), 5 m s^{-1} for radial wind (gray, dashed = inflow and solid = outflow), and 1 m s^{-1} for vertical velocity (black, dashed = downward motion and solid = upward motion). Note that there is no zero contour for radial wind and vertical velocity.

that was 5 km radially outward of an updraft and in a deep inflow layer, the downdraft here was too far from the strong updraft near 75-km radius (15 km radially inward of downdraft) to have an effect. Over the 2-h integration, no parcels that originated in this downdraft entered the updraft at 75-km radius. However, as a result of insufficient recovery, it is possible that the parcels' relatively low-θ_e values made it less likely for updrafts to initiate and strengthen during the 2-h integration.

Trajectories initially in the annulus confirm that the most unfavorable location of low-θ_e air is near the top of the inflow layer and slightly radially outward of updrafts. Of the 9095 trajectories that entered downdrafts, 914 entered an updraft (defined as 5 continuous minutes of the parcel experiencing greater than 1 m s^{-1} of upward motion) within 1 h of leaving the downdraft. Compared to θ_e values of the strongest updraft originally within 15 km radial distance of the downdraft (at the time parcels entered the downdraft), the mean θ_e deficit of these parcels as they enter the updraft is 5.9 K. The θ_e deficit is related to both the altitude of the downdraft parcels as they entered an updraft (Fig. 15a) and the downdraft's relative radial location to the updraft (Fig. 15b). The median θ_e deficit increases (parcel has a more negative effect) with increasing altitude of parcels as they enter the updraft, while it decreases with increasing original radial distance between the downdraft and the updraft. Both results indicate that the negative thermodynamic effects of downdrafts are maximized above 1500-m altitude and when the θ_e values have little time to recover before entering the updraft.

4) NONCONVECTIVE DOWNDRAFTS

While the focus of this study is on convective downdrafts, they take up a relatively small area of the storm. Nonconvective (e.g., broad subsidence) downdrafts near the boundary layer were also noticed, particularly in the broad area of low-θ_e air at 50-m altitude in the USL and USR quadrants of the Ideal3 simulation (Fig. 4a). Unsurprisingly, the boundary layer below 1-km altitude and between 100- and 150-km radius has significantly lower-θ_e air than air closer to the inner core (340–345 vs 350–355 K). With the broad distribution of low entropy air in the boundary layer, it only takes a relatively weak downdraft to transport the air to 50-m altitude or below. Cross sections in this region reveal that the presence of convection is limited and that boundary layer rolls are likely the catalyst for transporting low-θ_e air to 50 m (not shown).

Boundary layer rolls in TCs have been observed and simulated in regions away from deep convection (e.g., Wurman and Winslow 1998; Katsaros et al. 2000; Morrison et al. 2005; Foster 2005; Nolan 2005; Zhang et al. 2008; Lorsolo et al. 2008). An example of a boundary layer roll, alternating upward and downward motion with a wavelength of about 6 km that is mostly aligned with the wind field, is shown in Fig. 16. Trajectories from 64 parcels that originate in the downdraft part of the roll show two distinct horizontal solutions (Fig. 16d): one entrained in inflow and one closer to rotational motion (those above the inflow layer). By the end of the second hour, the parcels that are in the inflow layer (blue lines) enter the DSR quadrant, remain below 1500 m, and have a range of θ_e values between 346 and 354 K. The slow increase of θ_e leads to parcels having comparable values to the background air in the DSR quadrant (quadrant-averaged θ_e values are between 348 and 351 K at altitudes between 500 and 1500 m in Fig. 2d). While it is possible that entrainment and detrainment of air from parcels that originate in the rolls can influence the background θ_e values in this region, it is likely that the boundary layer rolls are sufficiently far away from the inner core such that air in the inflow layer associated with them can recover from the air–sea fluxes and poses no significant negative thermodynamic impact to the eyewall region.

4. Discussion and conclusions

This study used idealized TC simulations of category-3 (Ideal3) and category-5 (Ideal5) intensity to study the thermodynamic

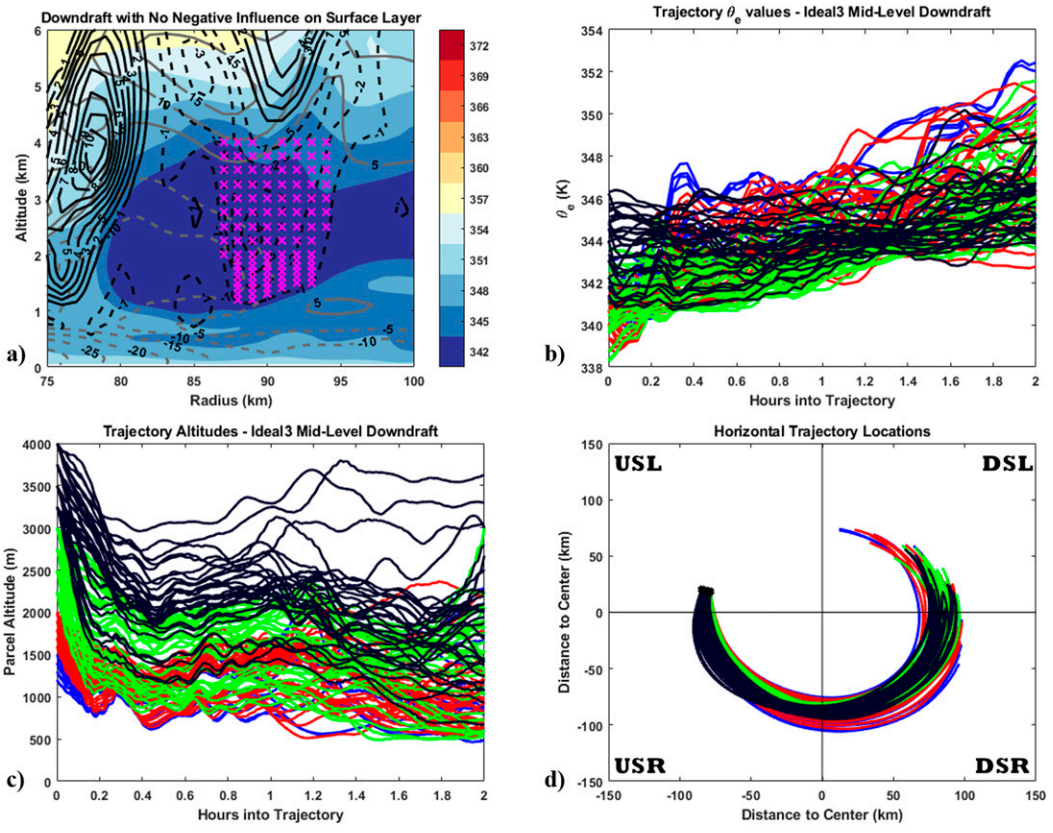

FIG. 14. As in Fig. 5, but for 108 parcel trajectories integrated over 2 h that were initially in a midlevel downdraft in Ideal3. The color of parcels is based on initial altitude (h_0) with blue: $1000 \leq h_0 \leq 1500$ m; red: $1500 < h_0 \leq 2000$ m; green: $2000 < h_0 \leq 3000$ m; and black: $h_0 > 3000$ m.

variability of downdrafts in TCs in relation to intensity, storm structure, and storm-relative location. While many studies have focused on the role of downdrafts in modulating TC intensity, to the authors' knowledge this is the first numerical study that diagnoses how downdraft characteristics are related to their influence on the boundary layer and nearby updrafts. Our significant findings are summarized in Fig. 17. In Ideal5 (Fig. 17a), well-organized eyewall updrafts transported high-θ_e air (>365 K) upward. The high-θ_e air was associated with low-level outflow from inside the eye and eye–eyewall mixing; downdrafts underneath the eyewall in this region (downdraft 1 in Fig. 17a) pose no negative thermodynamic influence to the boundary layer. Note that this moist-eyewall downdraft is similar to that identified using observations of Hurricane Earl (2010) in Wadler et al. (2018a) and is not the same as the quasi-stationary convective downdrafts in rainbands discussed by Riemer et al. (2010).

The layer of strong outflow between 1- and 2-km altitude extends to ~40 km radially outward from the eyewall, and was associated with higher θ_e values (~355 K) than typical for that radial range and altitude. The higher θ_e values initially appeared with the formation of a secondary eyewall feature 22 h before the analysis time and remained in place despite only the intermittent presence of outflow. Forward trajectories from convective downdrafts in this region (downdraft 2 in Fig. 17a) show that the favorably high-θ_e values (i.e., the amount of boundary layer recovery needed from downdrafts in this region is reduced) and associated convective stability in the outflow layer (i.e., increased stability reduces downward intrusions into the inflow layer) create a thermodynamic shield such that downdrafts have no negative thermodynamic impact to the boundary layer and eyewall updrafts. Some parcels descended to the inflow layer where their θ_e values increased from 353–355 K to 358–365 K as they spiraled inwards toward the eyewall. Parcels that stayed above the inflow layer traveled in nearly circular motion, maintained θ_e values between 350 and 355 K, and generally stayed below 2500-m altitude. The presence of a high-θ_e air above the inflow layer in Ideal5, which is also discussed in previous observational studies (e.g., Barnes 2008; Wadler et al. 2021), highlights the importance of storm structure in determining the thermodynamic effect of downdrafts. However, it remains unknown the exact mechanisms which lead to the formation of the high θ_e above the boundary layer in the TC and why this layer formed in Ideal5, but not in Ideal3. This will be a topic of future work.

For the convective downdrafts in Ideal3 (Fig. 17b), the radial location and altitude of a downdraft, relative to any nearby updrafts, is important for determining its effect on the boundary layer entropy and updraft thermal structure. A downdraft underneath the eyewall transported low-θ_e air to 400-m altitude (downdraft 1 in Fig. 17b). Since the low-θ_e air was below 500 m

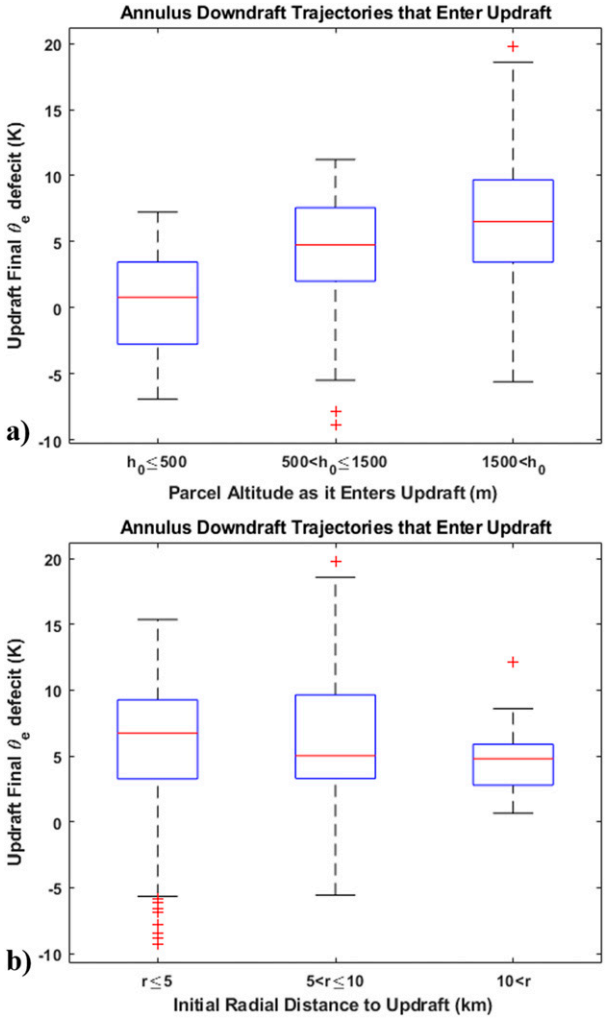

FIG. 15. Boxplots of updraft θ_e deficit (initial updraft θ_e values $-$ θ_e of parcels entering updrafts) for the parcels initiated in the annulus that entered downdrafts and subsequently entered an updraft. The θ_e deficit is relative to (a) altitude of parcels as they enter updraft and (b) initial radial distance between the parcel (as it enters the downdraft) and the closest updraft.

(approximate base of eyewall updrafts), the air moved radially inward below the eyewall and some recovery occurred near the eye. Parcels did not enter the eyewall until ~1.2 h into the trajectory integration, but still had a mean 5.2-K θ_e deficit compared to initial eyewall values. This partial recovery of θ_e in downdrafts parcels is further supported by trajectory analyses of thousands of parcels evenly distributed in an annulus around the storm. Parcels from the annulus that entered a downdraft and traveled underneath and radially inward of the eyewall generally increased their θ_e values (89% of them) 1 h after they entered the downdraft, but still had a mean 2.0-K θ_e deficit compared to initial eyewall values.

The downdrafts that lead to the most negative thermodynamic impact to updrafts are those that transport low-θ_e air from the midlevels to the top of the inflow layer (~1–1.5-km altitude) and just radially outward (~5 km) of the updraft core (downdraft 2 in Fig. 17b). The low-θ_e air at the top of the inflow layer can quickly travel to and enter the base of an updraft without undergoing much recovery. For the downdraft with the most negative influence to an updraft, the low-θ_e air entered the updraft with a mean θ_e deficit of 8.2 K compared to initial updraft values, less than 5 min after being transported downward. In contrast, a second midlevel downdraft was also analyzed transporting low θ_e from the midtroposphere downward (downdraft 4 in Fig. 17b), but unlike the previously discussed downdraft that appears to weaken the TC intensity, this convective downdraft was directly underneath the base of an updraft without significant radial tilt (and 15 km from the nearest radially inward updraft). Parcels from this downdraft entered the top of the inflow layer (traveling inward away from the updraft), experienced small recovery (average θ_e increase of 2.5 K over the first hour), but did not enter an updraft within the 2-h trajectory integration (though the low-θ_e values could have prevented future updrafts from forming).

The parcels initiated in the annulus that entered a downdraft followed by entering an updraft (within 1 h of leaving the downdraft) support this result. The median θ_e deficit (reduction of updraft θ_e value by the parcel) was largest for parcels that entered the updraft above 1500 m and was lowest for parcels that entered the updraft below 500 m. The median θ_e deficit was also maximized when parcels entered the updraft within 5-km radial distance. The θ_e deficit was reduced when the radial distance was between 5 and 10 km. Together, the results signify that for a downdraft to negatively influence an updraft, it cannot be directly underneath the updraft (unfavorable air will travel radially inward away from the updraft) or greater than ~10 km radially outward from the updraft (air will take too long to reach updraft and will likely experience significant recovery in the inflow layer). The importance of the relative radial location between the downdraft and updraft implies that the radial tilt of the updraft plays a role in determining if the updraft will be influenced by low-θ_e downdrafts.

Another interesting result from Ideal3 is that most convective downdrafts transported air to the top of the inflow layer (~500-m–1-km altitude), where parcels could not recover via the air–sea enthalpy fluxes. From all the cross sections analyzed in this study, only convective downdrafts with its fastest downward vertical velocity in the lowest 1 km brought low-θ_e air to the near-surface layer (e.g., downdraft 3 in Fig. 17b). While low θ_e near the sea surface initially appeared most unfavorable, in both simulations parcels near 300-m altitude outside of the eyewall experienced heating rates of 12–15 K h^{-1} due to the air–sea enthalpy fluxes and turbulent mixing with high-entropy air near the sea surface.

With boundary layer recovery a recurring theme for parcels that enter the inflow layer, the θ_e values at 1 h into the trajectories were strongly dependent on the minimum altitude they attained (Fig. 18). In Ideal3, both for parcels initiated directly in downdrafts (Fig. 18a) and for those initiated in the annulus (Fig. 18c), the correlation (r) between minimum parcel altitude and θ_e at 1 h into trajectories for parcels initiated in downdrafts is -0.72 (parcels

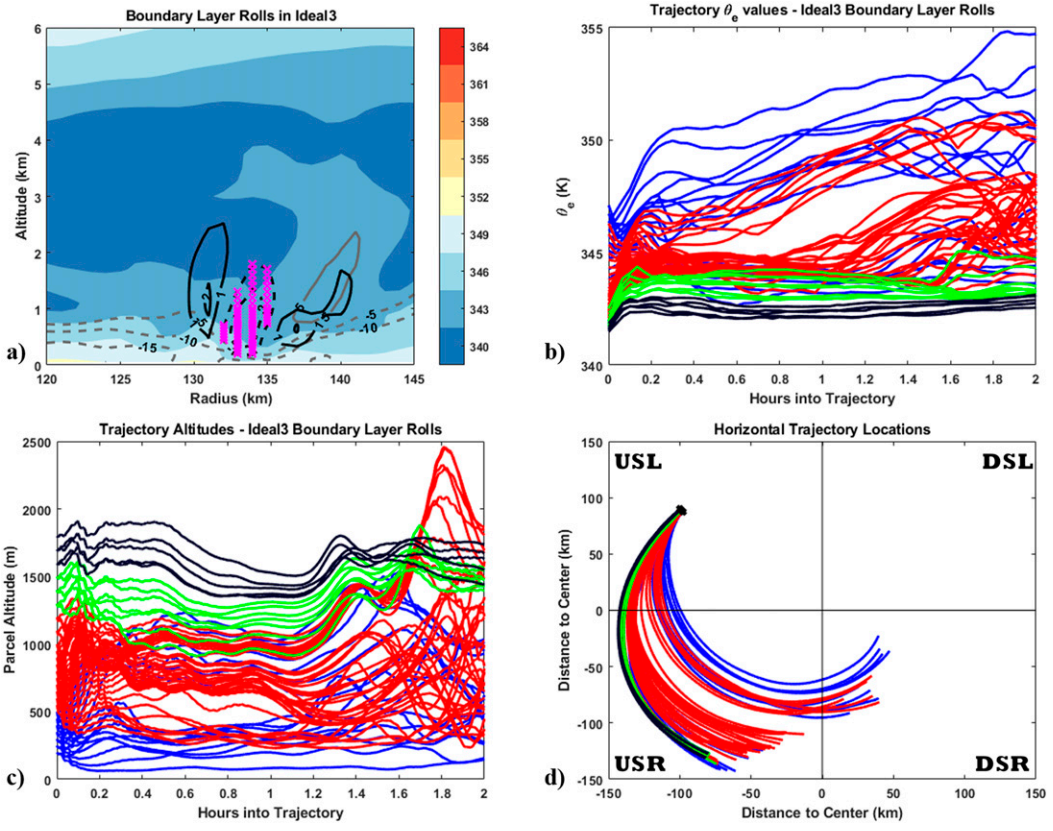

FIG. 16. As in Fig. 5, but for 64 parcel trajectories integrated over 2 h that were initially in a boundary layer roll in Ideal3. Note that the color scale in (a) is different from all the previous figures. The color of parcels is based on initial altitude (h_0) with blue: $200 \leq h_0 \leq 500$ m; red: $500 < h_0 \leq 1250$ m; green: $1250 < h_0 \leq 1500$ m; and black: $h_0 > 1500$ m.

from Ideal5 are not included since they create a separate data cluster which creates a misleadingly high correlation coefficient). Additionally, parcels that descended below 500 m always achieved θ_e greater than 348 K, while parcels that did not descend below 2000-m altitude never achieved θ_e greater than 348 K. The correlation for parcels initiated in the annulus is −0.66 for those that descended below 1500 m (Fig. 18c). This cannot be explained by the parcel's initial location as the initial θ_e of parcels is only weakly correlated to their initial altitude ($r = -0.25$ in Fig. 18b; $r = -0.15$; Fig. 18d). Instead, this correlation indicates that the air–sea enthalpy fluxes and turbulent mixing with the higher-θ_e air in the boundary layer are the primary controls for the thermodynamic evolution of air parcels originally embedded in downdrafts. Despite their possibly very low initial θ_e values, parcels are able to sufficiently recover over the first hour of the trajectories toward more typical θ_e values for that altitude. Note that there is very weak correlation for parcels above 1500 m, signifying that the air–sea interactions do not influence the recovery process above this altitude. No significant correlations were found between the θ_e value of parcels with their initial or final radius.

Last, in Ideal3, there was a ring of low-θ_e air (~345 K) at 50-m altitude between 150- and 200-km radius that was associated with generally unfavorable boundary layer air far away from the storm. This air was brought to the near-surface layer by boundary layer rolls (convective downdrafts are sparse this far away from storm center). While this air initially looks unfavorable, parcel trajectories show that the air is sufficiently far away from the eyewall such that, as it spirals inwards, the air is able to sufficiently recover via the air sea enthalpy fluxes.

Overall, this study documents that the impact of downdrafts on boundary layer thermodynamics depends on the background θ_e distribution that is affected by storm strength and vortex structure. In the absence of the downdraft occurring in a region of favorably high-θ_e values, the θ_e deficit is controlled by the minimum height of the downdraft (greatest deficit near the top of the inflow layer) and the radial location of the downdraft relative to the updraft (greatest deficit within 5-km radial distance). This numerical study builds upon the recent observational case studies of Zawislak et al. (2016), Nguyen et al. (2017), and Wadler et al. (2018a) that studied the thermodynamic impact of downdrafts on TC structure and intensity, and the numerical study by Alland et al. (2021a) which studied the pathways for which downdraft ventilation can weaken a TC. What remains unclear is the exact mechanism by which each downdraft influences TC intensity (or if they do at all). With

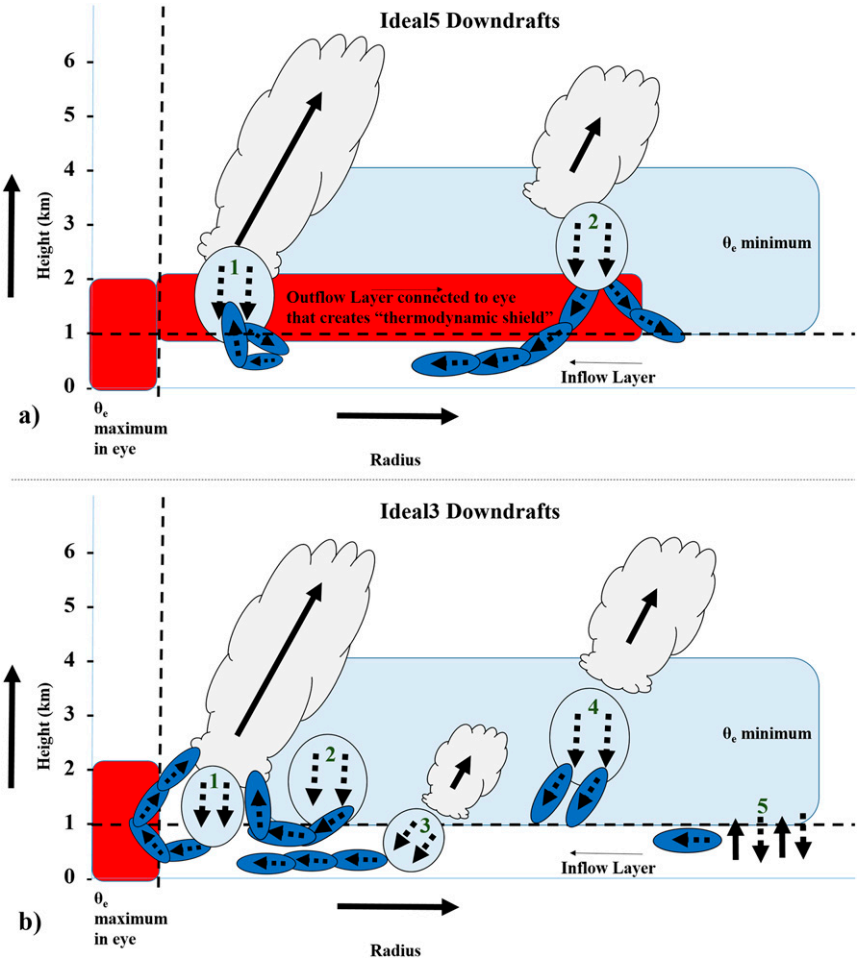

FIG. 17. Radius–height cross-section summary schematic of the thermodynamic impact that downdrafts have in (a) Ideal5 and (b) Ideal3. In both panels updrafts are indicated by clouds, downdrafts are indicated by dashed down arrows in a light blue circle, and parcel trajectory locations are indicated by dashed arrows in dark blue circles. The downdrafts are numbered for reference in the text. The midtropospheric minimum in θ_e is indicated in light blue and the high θ_e in the eye and low-level outflow in (a) is indicated in red.

hundreds of distinct downdrafts at any given time, it is difficult to discern how any individual cell influences the storm intensity. However, with distinct characteristics of each downdraft determining their effects, future studies can analyze whether certain storm and environmental characteristics change the relative distribution of favorable and unfavorable downdrafts.

With downdrafts that transport low-θ_e air to the top of the inflow layer (~1–1.5-km altitude) documented as the most thermodynamically unfavorable for the boundary layer and nearby updrafts, future work should investigate which downdraft signatures lead to changes in the radial gradient of θ_e in the eyewall region, which is a factor in potential intensity theory (Emanuel 1988). Additionally, since the focus of this study is on relatively strong TCs in moderate wind shear regimes ($5\,m\,s^{-1}$ in Ideal5 and $10\,m\,s^{-1}$ in Ideal3), future work should also study the effects of downdrafts in weaker TCs embedded in stronger environmental wind shear. The weaker TCs often have less organized circulations and the higher wind shear values can lead a greater vortex tilt and potentially a different spatial distribution of downdrafts (as alluded to in Riemer et al. 2010), which may modify the thermodynamic effects of individual downdrafts. Last, more work is needed to understand how downdrafts influence the radial and azimuthal distribution of convection, which have both been linked to TC intensity changes (e.g., Kelley et al. 2004; Hendricks et al. 2004; Braun et al. 2006; Montgomery et al. 2006; Reasor et al. 2009; Guimond et al. 2010; Rogers et al. 2013b, 2015, 2016; Stevenson et al. 2014; Wadler et al. 2018b). This can be performed with numerical simulations that have realistic environmental conditions to account for moisture gradients that can drastically change downdraft characteristics. Nevertheless, the results from this study emphasize that there are significant variations in downdraft characteristics and their influence on the boundary layer which must be taken into consideration when evaluating how downdrafts influence storm intensity.

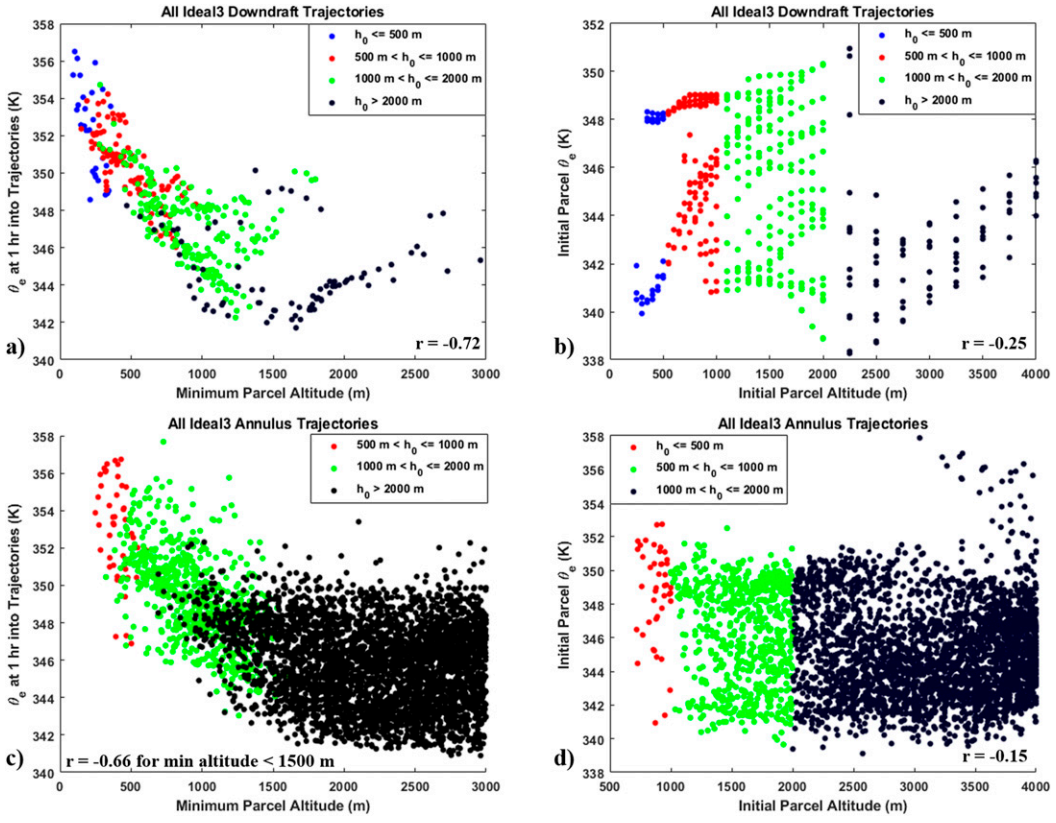

FIG. 18. Scatterplots from all trajectories initialized directly into downdrafts in Ideal3 of (a) minimum parcel altitude through the first hour of trajectories with the θ_e at 1 h into the trajectories and (b) initial parcel altitude with initial parcel θ_e. (c),(d) As in (a) and (b), but for parcels initialized in the annulus that entered downdrafts. The points are colored based on initial altitude with blue: $h_0 \leq 500$ m; red: $500 < h_0 \leq 1000$ m; green: $1000 < h_0 \leq 2000$ m; and black: $h_0 > 2000$ m. The r value in the bottom right of each panel is the Pearson correlation coefficient.

Acknowledgments. The authors are grateful for the comments and suggestions from three anonymous reviewers. This work was completed while Joshua Wadler was gratefully supported by the National Science Foundation Graduate Research Fellowship under Grant DGE-1451511. David Nolan was supported by the NASA *CloudSat*/*CALIPSO* Scene Team Program under Grant NNXW1GAP19G. Jun Zhang was supported by NSF Grant AGS1822128, NOAA Grant NA19OAR4590239, and ONR Grant N00014-20-1-2071. Lynn Shay gratefully acknowledges support by the National Science Foundation under Grant AGS 19-41498. Computational time was generously provided by the Institute for Data Science and Computing (IDSC) at the University of Miami. The authors are grateful to NCAR-MMM for making the WRF Model freely available.

REFERENCES

Alland, J. J., B. H. Tang, and K. L. Corbosiero, 2017: Effects of midlevel dry air on development of the axisymmetric tropical cyclone secondary circulation. *J. Atmos. Sci.*, **74**, 1455–1470, https://doi.org/10.1175/JAS-D-16-0271.1.

——, ——, ——, and G. H. Bryan, 2021a: Combined effects of midlevel dry air and vertical wind shear on tropical cyclone development. Part I: Downdraft ventilation. *J. Atmos. Sci.*, **78**, 763–782, https://doi.org/10.1175/JAS-D-20-0054.1.

——, ——, ——, and ——, 2021b: Combined effects of midlevel dry air and vertical wind shear on tropical cyclone development. Part II: Radial ventilation. *J. Atmos. Sci.*, **78**, 783–796, https://doi.org/10.1175/JAS-D-20-0055.1.

Balaguru, K., G. R. Foltz, L. R. Leung, J. Kaplan, W. Xu, N. Reul, and B. Chapron, 2020: Pronounced impact of salinity on rapidly intensifying tropical cyclones. *Bull. Amer. Meteor. Soc.*, **101**, E1497–E1511, https://doi.org/10.1175/BAMS-D-19-0303.1.

Barnes, G. M., 2008: Atypical thermodynamic profiles in hurricanes. *Mon. Wea. Rev.*, **136**, 631–643, https://doi.org/10.1175/2007MWR2033.1.

——, and M. D. Powell, 1995: Evolution of the inflow boundary layer of Hurricane Gilbert (1988). *Mon. Wea. Rev.*, **123**, 2348–2368, https://doi.org/10.1175/1520-0493(1995)123<2348:EOTIBL>2.0.CO;2.

——, and P. Fuentes, 2010: Eye excess energy and the rapid intensification of Hurricane Lili (2002). *Mon. Wea. Rev.*, **138**, 1015–1027, https://doi.org/10.1175/2009MWR3145.1.

——, and K. P. Dolling, 2013: The inflow to Tropical Cyclone Humberto (2001) as viewed with azimuth–height surfaces over three days. *Mon. Wea. Rev.*, **141**, 1324–1336, https://doi.org/10.1175/MWR-D-11-00348.1.

——, E. J. Zipser, D. Jorgensen, and F. D. Marks, 1983: Mesoscale and convective structure of a hurricane rainband. *J. Atmos. Sci.*, **40**, 2125–2137, https://doi.org/10.1175/1520-0469(1983)040<2125:MACSOA>2.0.CO;2.

Bolton, D., 1980: The computation of equivalent potential temperature. *Mon. Wea. Rev.*, **108**, 1046–1053, https://doi.org/10.1175/1520-0493(1980)108<1046:TCOEPT>2.0.CO;2.

Braun, S. A., M. T. Montgomery, and Z. Pu, 2006: High-resolution simulation of Hurricane Bonnie (1998). Part I: The organization of eyewall vertical motion. *J. Atmos. Sci.*, **63**, 19–42, https://doi.org/10.1175/JAS3598.1.

Cangialosi, J. P., E. Blake, M. DeMaria, A. Penny, A. Latto, E. Rappaport, and V. Tallapragada, 2020: Recent progress in tropical cyclone intensity forecasting at the National Hurricane Center. *Wea. Forecasting*, **35**, 1913–1922, https://doi.org/10.1175/WAF-D-20-0059.1.

Cione, J. J., P. G. Black, and S. H. Houston, 2000: Surface observations in the hurricane environment. *Mon. Wea. Rev.*, **128**, 1550–1561, https://doi.org/10.1175/1520-0493(2000)128<1550:SOITHE>2.0.CO;2.

——, E. A. Kalina, J. A. Zhang, and E. W. Uhlhorn, 2013: Observations of air–sea interaction and intensity change in hurricanes. *Mon. Wea. Rev.*, **141**, 2368–2382, https://doi.org/10.1175/MWR-D-12-00070.1.

Colomb, A., T. Kriat, and M. Leroux, 2019: On the rapid weakening of very intense Tropical Cyclone Hellen (2014). *Mon. Wea. Rev.*, **147**, 2717–2737, https://doi.org/10.1175/MWR-D-18-0309.1.

Cram, T. A., J. Persing, M. T. Montgomery, and S. A. Braun, 2007: A Lagrangian trajectory view on transport and mixing processes between the eye, eyewall, and environment using a high-resolution simulation of Hurricane Bonnie (1998). *J. Atmos. Sci.*, **64**, 1835–1856, https://doi.org/10.1175/JAS3921.1.

DeHart, J. C., R. A. Houze Jr., and R. F. Rogers, 2014: Quadrant distribution of tropical cyclone inner-core kinematics in relation to environmental shear. *J. Atmos. Sci.*, **71**, 2713–2732, https://doi.org/10.1175/JAS-D-13-0298.1.

DeMaria, M., C. R. Sampson, J. A. Knaff, and K. D. Musgrave, 2014: Is tropical cyclone intensity guidance improving? *Bull. Amer. Meteor. Soc.*, **95**, 387–398, https://doi.org/10.1175/BAMS-D-12-00240.1.

——, J. L. Franklin, M. J. Onderlinde, and J. Kaplan, 2021: Operational forecasting of tropical cyclone rapid intensification at the National Hurricane Center. *Atmosphere*, **12**, 683, https://doi.org/10.3390/atmos12060683.

Didlake, A. C., Jr., and R. A. Houze Jr., 2009: Convective-scale downdrafts in the principal rainband of Hurricane Katrina (2005). *Mon. Wea. Rev.*, **137**, 3269–3293, https://doi.org/10.1175/2009MWR2827.1.

——, and ——, 2013: Dynamics of the stratiform sector of a tropical cyclone rainband. *J. Atmos. Sci.*, **70**, 1891–1911, https://doi.org/10.1175/JAS-D-12-0245.1.

Dolling, K. P., and G. M. Barnes, 2012: The creation of a high equivalent potential temperature reservoir in Tropical Storm Humberto (2001) and its possible role in storm deepening. *Mon. Wea. Rev.*, **140**, 492–505, https://doi.org/10.1175/MWR-D-11-00068.1.

——, and ——, 2014: The evolution of Hurricane Humberto (2001). *J. Atmos. Sci.*, **71**, 1276–1291, https://doi.org/10.1175/JAS-D-13-0164.1.

Dunion, J. P., 2011: Rewriting the climatology of the tropical North Atlantic and Caribbean Sea atmosphere. *J. Climate*, **24**, 893–908, https://doi.org/10.1175/2010JCLI3496.1.

Eastin, M. D., T. L. Gardner, M. C. Link, and K. C. Smith, 2012: Surface cold pools in the outer rainbands of Tropical Storm Hanna (2008) near landfall. *Mon. Wea. Rev.*, **140**, 471–491, https://doi.org/10.1175/MWR-D-11-00099.1.

Emanuel, K. A., 1988: The maximum intensity of hurricanes. *J. Atmos. Sci.*, **45**, 1143–1155, https://doi.org/10.1175/1520-0469(1988)045<1143:TMIOH>2.0.CO;2.

Foster, R. C., 2005: Why rolls are prevalent in the hurricane boundary layer. *J. Atmos. Sci.*, **62**, 2647–2661, https://doi.org/10.1175/JAS3475.1.

Ge, X., T. Li, and M. Peng, 2013: Effects of vertical shears and midlevel dry air on tropical cyclone developments. *J. Atmos. Sci.*, **70**, 3859–3875, https://doi.org/10.1175/JAS-D-13-066.1.

Guimond, S. R., G. M. Heymsfield, and F. J. Turk, 2010: Multiscale observations of Hurricane Dennis (2005): The effects of hot towers on rapid intensification. *J. Atmos. Sci.*, **67**, 633–654, https://doi.org/10.1175/2009JAS3119.1.

Hawkins, H. F., and S. M. Imbembo, 1976: The structure of a small, intense hurricane—Inez 1966. *Mon. Wea. Rev.*, **104**, 418–442, https://doi.org/10.1175/1520-0493(1976)104<0418:TSOASI>2.0.CO;2.

Hendricks, E. A., M. T. Montgomery, and C. A. Davis, 2004: The role of "vortical" hot towers in the formation of Tropical Cyclone Diana (1984). *J. Atmos. Sci.*, **61**, 1209–1232, https://doi.org/10.1175/1520-0469(2004)061<1209:TROVHT>2.0.CO;2.

Hlywiak, J., and D. S. Nolan, 2019: The influence of oceanic barrier layers on tropical cyclone intensity as determined through idealized, coupled numerical simulations. *J. Phys. Oceanogr.*, **49**, 1723–1745, https://doi.org/10.1175/JPO-D-18-0267.1.

Hong, S.-Y., Y. Noh, and J. Dudhia, 2006: A new vertical diffusion package with an explicit treatment of entrainment processes. *Mon. Wea. Rev.*, **134**, 2318–2341, https://doi.org/10.1175/MWR3199.1.

Iacono, M. J., J. S. Delamere, E. J. Mlawer, M. W. Shephard, S. A. Clough, and W. D. Collins, 2008: Radiative forcing by long-lived greenhouse gases: Calculations with the AER radiative transfer models. *J. Geophys. Res.*, **113**, D13103, https://doi.org/10.1029/2008JD009944.

Jaimes, B., and L. K. Shay, 2009: Mixed layer cooling in mesoscale oceanic eddies during Hurricanes Katrina and Rita. *Mon. Wea. Rev.*, **137**, 4188–4207, https://doi.org/10.1175/2009MWR2849.1.

——, and ——, 2010: Near-inertial wave wake of Hurricanes Katrina and Rita over mesoscale oceanic eddies. *J. Phys. Oceanogr.*, **40**, 1320–1337, https://doi.org/10.1175/2010JPO4309.1.

——, ——, and E. W. Uhlhorn, 2015: Enthalpy and momentum fluxes during Hurricane Earl relative to underlying ocean features. *Mon. Wea. Rev.*, **143**, 111–131, https://doi.org/10.1175/MWR-D-13-00277.1.

Katsaros, K. B., P. W. Vachon, P. G. Black, P. P. Dodge, and E. W. Uhlhorn, 2000: Wind fields from SAR: Could they im-prove our understanding of storm dynamics? *Johns Hopkins APL Tech. Dig.*, **211**, 86–93, https://doi.org/10.4095/219617.

Kelley, O. A., J. Stout, and J. B. Halverson, 2004: Tall precipitation cells in tropical cyclone eyewalls are associated with tropical cyclone intensification. *Geophys. Res. Lett.*, **31**, L24112, https://doi.org/10.1029/2004GL021616.

Klotz, B. W., and D. S. Nolan, 2019: SFMR surface wind undersampling over the tropical cyclone life cycle. *Mon. Wea. Rev.*, **147**, 247–268, https://doi.org/10.1175/MWR-D-18-0296.1.

Li, Q., and Y. Dai, 2020: Revisiting azimuthally asymmetric moist instability in the outer core of sheared tropical cyclones. *Mon. Wea. Rev.*, **148**, 1297–1319, https://doi.org/10.1175/MWR-D-19-0004.1.

Lim, K.-S. S., and S.-Y. Hong, 2010: Development of an effective double-moment cloud microphysics scheme with prognostic

cloud condensation nuclei (CCN) for weather and climate models. *Mon. Wea. Rev.*, **138**, 1587–1612, https://doi.org/10.1175/2009MWR2968.1.

Lorsolo, S., J. L. Schroeder, P. Dodge, and F. Marks Jr., 2008: An observational study of hurricane boundary layer small-scale coherent structures. *Mon. Wea. Rev.*, **136**, 2871–2893, https://doi.org/10.1175/2008MWR2273.1.

Marks, F. D., and L. K. Shay, 1998: Landfalling tropical cyclones: Forecast problems and associated research opportunities. *Bull. Amer. Meteor. Soc.*, **79**, 305–323, https://doi.org/10.1175/1520-0477(1998)079<0285:QPFROT>2.0.CO;2.

Molinari, J., J. Frank, and D. Vollaro, 2013: Convective bursts, downdraft cooling, and boundary layer recovery in a sheared tropical storm. *Mon. Wea. Rev.*, **141**, 1048–1060, https://doi.org/10.1175/MWR-D-12-00135.1.

Montgomery, M. T., M. Nicholls, T. Cram, and A. Saunders, 2006: A "vortical" hot tower route to tropical cyclogenesis. *J. Atmos. Sci.*, **63**, 355–386, https://doi.org/10.1175/JAS3604.1.

Moon, Y., and D. S. Nolan, 2015: Spiral rainbands in a numerical simulation of Hurricane Bill (2009). Part I: Structures and comparisons to observations. *J. Atmos. Sci.*, **72**, 164–190, https://doi.org/10.1175/JAS-D-14-0058.1.

Morrison, I., S. Businger, F. Marks, P. Dodge, and J. A. Businger, 2005: An observational case for the prevalence of roll vortices in the hurricane boundary layer. *J. Atmos. Sci.*, **62**, 2662–2673, https://doi.org/10.1175/JAS3508.1.

Nguyen, L. T., R. F. Rogers, and P. D. Reasor, 2017: Thermodynamic and kinematic influences on precipitation symmetry in sheared tropical cyclones: Bertha and Cristobal (2014). *Mon. Wea. Rev.*, **145**, 4423–4446, https://doi.org/10.1175/MWR-D-17-0073.1.

——, ——, J. Zawislak, and J. A. Zhang, 2019: Assessing the influence of convective downdrafts and surface enthalpy fluxes on tropical cyclone intensity change in moderate vertical wind shear. *Mon. Wea. Rev.*, **147**, 3519–3534, https://doi.org/10.1175/MWR-D-18-0461.1.

Noh, Y., W. G. Cheon, S. Y. Hong, and S. Raasch, 2003: Improvement of the K-profile model for the planetary boundary layer based on large eddy simulation data. *Bound.-Layer Meteor.*, **107**, 421–427, https://doi.org/10.1023/A:1022146015946.

Nolan, D. S., 2005: Instabilities in hurricane-like boundary layers. *Dyn. Atmos. Oceans*, **40**, 209–236, https://doi.org/10.1016/j.dynatmoce.2005.03.002.

——, D. P. Stern, and J. A. Zhang, 2009: Evaluation of planetary boundary layer parameterizations in tropical cyclones by comparison of in situ observations and high-resolution simulations of Hurricane Isabel (2003). Part II: Inner-core boundary layer and eyewall structure. *Mon. Wea. Rev.*, **137**, 3675–3698, https://doi.org/10.1175/2009MWR2786.1.

——, R. Atlas, K. T. Bhatia, and L. R. Bucci, 2013: Development and validation of a hurricane nature run using the joint OSSE nature run and the WRF Model. *J. Adv. Model. Earth Syst.*, **5**, 382–405, https://doi.org/10.1002/jame.20031.

Onderlinde, M. J., and D. S. Nolan, 2016: Tropical cyclone–relative environmental helicity and the pathways to intensification in shear. *J. Atmos. Sci.*, **73**, 869–890, https://doi.org/10.1175/JAS-D-15-0261.1.

Pollard, R. T., P. B. Rhines, and R. O. R. Y. Thompson, 1973: The deepening of the wind-mixed layer. *Geophys. Fluid Dyn.*, **3**, 381–404, https://doi.org/10.1080/03091927208236105.

Powell, M. D., 1990: Boundary layer structure and dynamics in outer hurricane rainbands. Part II: Downdraft modification and mixed layer recovery. *Mon. Wea. Rev.*, **118**, 918–938, https://doi.org/10.1175/1520-0493(1990)118<0918:BLSADI>2.0.CO;2.

Reasor, P. D., M. D. Eastin, and J. F. Gamache, 2009: Rapidly intensifying Hurricane Guillermo (1997). Part I: Low-wavenumber structure and evolution. *Mon. Wea. Rev.*, **137**, 603–631, https://doi.org/10.1175/2008MWR2487.1.

——, R. F. Rogers, and S. Lorsolo, 2013: Environmental flow impacts on tropical cyclone structure diagnosed from airborne Doppler radar composites. *Mon. Wea. Rev.*, **141**, 2949–2969, https://doi.org/10.1175/MWR-D-12-00334.1.

Riemer, M., M. T. Montgomery, and M. E. Nicholls, 2010: A new paradigm for intensity modification of tropical cyclones: Thermodynamic impact of vertical wind shear on the inflow layer. *Atmos. Chem. Phys.*, **10**, 3163–3188, https://doi.org/10.5194/acp-10-3163-2010.

——, ——, and ——, 2013: Further examination of the thermodynamic modification of the inflow layer of tropical cyclones by vertical wind shear. *Atmos. Chem. Phys.*, **13**, 327–346, https://doi.org/10.5194/acp-13-327-2013.

Rogers, R., and Coauthors, 2006: The Intensity Forecasting Experiment: A NOAA multiyear field program for improving tropical cyclone intensity forecasts. *Bull. Amer. Meteor. Soc.*, **87**, 1523–1538, https://doi.org/10.1175/BAMS-87-11-1523.

——, and Coauthors, 2013a: NOAA's hurricane Intensity Forecasting Experiment: A progress report. *Bull. Amer. Meteor. Soc.*, **94**, 859–882, https://doi.org/10.1175/BAMS-D-12-00089.1.

——, P. D. Reasor, and S. Lorsolo, 2013b: Airborne Doppler observations of the inner-core structural differences between intensifying and steady-state tropical cyclones. *Mon. Wea. Rev.*, **141**, 2970–2991, https://doi.org/10.1175/MWR-D-12-00357.1.

——, ——, and J. A. Zhang, 2015: Multiscale structure and evolution of Hurricane Earl (2010) during rapid intensification. *Mon. Wea. Rev.*, **143**, 536–562, https://doi.org/10.1175/MWR-D-14-00175.1.

——, J. A. Zhang, J. Zawislak, H. Jiang, G. R. Alvey III, E. J. Zipser, and S. N. Stevenson, 2016: Observations of the structure and evolution of Hurricane Edouard (2014) during intensity change. Part II: Kinematic structure and the distribution of deep convection. *Mon. Wea. Rev.*, **144**, 3355–3376, https://doi.org/10.1175/MWR-D-16-0017.1.

Rotunno, R., and K. A. Emanuel, 1987: An air–sea interaction theory for tropical cyclones. Part II: Evolutionary study using a nonhydrostatic axisymmetric numerical model. *J. Atmos. Sci.*, **44**, 542–561, https://doi.org/10.1175/1520-0469(1987)044<0542:AAITFT>2.0.CO;2.

Rudzin, J. E., L. K. Shay, and W. E. Johns, 2018: The influence of the barrier layer on SST response during tropical cyclone wind forcing using idealized experiments. *J. Phys. Oceanogr.*, **48**, 1471–1478, https://doi.org/10.1175/JPO-D-17-0279.1.

——, ——, and B. Jaimes de la Cruz, 2019: The impact of the Amazon–Orinoco River plume on enthalpy flux and air–sea interaction within Caribbean Sea tropical cyclones. *Mon. Wea. Rev.*, **147**, 931–950, https://doi.org/10.1175/MWR-D-18-0295.1.

——, S. Chen, E. R. Sanabia, and S. R. Jayne, 2020: The air-sea response during Hurricane Irma's (2017) rapid intensification over the Amazon-Orinoco River plume as measured by atmospheric and oceanic observations. *J. Geophys. Res. Atmos.*, **125**, e2019JD032368, https://doi.org/10.1029/2019JD032368.

Shay, L. K., G. J. Goni, and P. G. Black, 2000: Effects of a warm oceanic feature on Hurricane Opal. *Mon. Wea. Rev.*, **128**, 1366–1383, https://doi.org/10.1175/1520-0493(2000)128<1366:EOAWOF>2.0.CO;2.

Skamarock, W. C., and Coauthors, 2008: A description of the Advanced Research WRF version 3. NCAR Tech. Note

NCAR/TN-475+STR, 113 pp., https://doi.org/10.5065/D68S4MVH.

Stevenson, S. N., K. L. Corbosiero, and J. Molinari, 2014: The convective evolution and rapid intensification of Hurricane Earl (2010). *Mon. Wea. Rev.*, **142**, 4364–4380, https://doi.org/10.1175/MWR-D-14-00078.1.

Tang, B., and K. Emanuel, 2010: Midlevel ventilation's constraint on tropical cyclone intensity. *J. Atmos. Sci.*, **67**, 1817–1830, https://doi.org/10.1175/2010JAS3318.1.

——, and ——, 2012: Sensitivity of tropical cyclone intensity to ventilation in an axisymmetric model. *J. Atmos. Sci.*, **69**, 2394–2413, https://doi.org/10.1175/JAS-D-11-0232.1.

Tiedtke, M., 1989: A comprehensive mass flux scheme for cumulus parameterization in large-scale models. *Mon. Wea. Rev.*, **117**, 1779–1800, https://doi.org/10.1175/1520-0493(1989)117<1779:ACMFSF>2.0.CO;2.

Trabing, B. C., and M. M. Bell, 2020: Understanding error distributions of hurricane intensity forecasts during rapid intensity changes. *Wea. Forecasting*, **35**, 2219–2234, https://doi.org/10.1175/WAF-D-19-0253.1.

Wadler, J. B., J. A. Zhang, B. Jaimes, and L. K. Shay, 2018a: Downdrafts and the evolution of boundary layer thermodynamics in Hurricane Earl (2010) before and during rapid intensification. *Mon. Wea. Rev.*, **146**, 3545–3565, https://doi.org/10.1175/MWR-D-18-0090.1.

——, R. F. Rogers, and P. D. Reasor, 2018b: The relationship between spatial variations in the structure of convective bursts and tropical cyclone intensification as determined by airborne Doppler radar. *Mon. Wea. Rev.*, **146**, 761–780, https://doi.org/10.1175/MWR-D-17-0213.1.

——, J. A. Zhang, R. F. Rogers, B. Jaimes, and L. K. Shay, 2021: The rapid intensification of Hurricane Michael (2018): Storm structure and the relationship to environmental and air–sea interactions. *Mon. Wea. Rev.*, **149**, 245–267, https://doi.org/10.1175/MWR-D-20-0145.1.

Wang, Y., J. D. Kepert, and G. J. Holland, 2001: The effect of sea spray evaporation on tropical cyclone boundary layer structure and intensity. *Mon. Wea. Rev.*, **129**, 2481–2500, https://doi.org/10.1175/1520-0493(2001)129<2481:TEOSSE>2.0.CO;2.

Wroe, D. R., and G. M. Barnes, 2003: Inflow layer energetics of Hurricane Bonnie (1998) near landfall. *Mon. Wea. Rev.*, **131**, 1600–1612, https://doi.org/10.1175//2547.1.

Wurman, J., and J. Winslow, 1998: Intense sub-kilometer boundary layer rolls in Hurricane Fran. *Science*, **280**, 555–557, https://doi.org/10.1126/science.280.5363.555.

Zawislak, J., H. Jiang, G. Alvey, E. Zipser, R. Rogers, J. Zhang, and S. Stevenson, 2016: Observations of the structure and evolution of Hurricane Edouard (2014) during intensity change. Part I: Relationship between the thermodynamic structure and precipitation. *Mon. Wea. Rev.*, **144**, 3333–3354, https://doi.org/10.1175/MWR-D-16-0018.1.

——, and Coauthors, 2021: Accomplishments of NOAA's airborne Hurricane Field Program and a broader future approach to forecast improvement. *Bull. Amer. Meteor. Soc.*, **102**, 1–79, https://doi.org/10.1175/BAMS-D-20-0174.1.

Zhang, C., Y. Wang, and K. Hamilton, 2011: Improved representation of boundary layer clouds over the Southeast Pacific in ARW-WRF using a modified Tiedtke cumulus parameterization scheme. *Mon. Wea. Rev.*, **139**, 3489–3513, https://doi.org/10.1175/MWR-D-10-05091.1.

Zhang, D.-L., Y. Liu, and M. K. Yau, 2000: A multiscale numerical study of Hurricane Andrew (1992). Part III: Dynamically induced vertical motion. *Mon. Wea. Rev.*, **128**, 3772–3788, https://doi.org/10.1175/1520-0493(2001)129<3772:AMNSOH>2.0.CO;2.

——, ——, and ——, 2001: A multiscale numerical study of Hurricane Andrew (1992). Part IV: Unbalanced flows. *Mon. Wea. Rev.*, **129**, 92–107, https://doi.org/10.1175/1520-0493(2001)129<0092:AMNSOH>2.0.CO;2.

Zhang, J. A., K. B. Katsaros, P. G. Black, S. Lehner, J. R. French, and W. M. Drennan, 2008: Effects of roll vortices on turbulent fluxes in the hurricane boundary layer. *Bound.-Layer Meteor.*, **128**, 173–189, https://doi.org/10.1007/s10546-008-9281-2.

——, R. Rogers, P. Reasor, E. Uhlhorn, and F. Marks, 2013: Asymmetric hurricane boundary layer structure from dropsonde composites in relation to the environmental vertical wind shear. *Mon. Wea. Rev.*, **141**, 3968–3984, https://doi.org/10.1175/MWR-D-12-00335.1.

——, J. J. Cione, E. A. Kalina, E. W. Uhlhorn, T. Hock, and J. A. Smith, 2017: Observations of infrared sea surface temperature and air–sea interaction in Hurricane Edouard (2014) using GPS dropsondes. *J. Atmos. Oceanic Technol.*, **34**, 1333–1349, https://doi.org/10.1175/JTECH-D-16-0211.1.